Annexe A

PDMS-based microfluidics for proteomic analysis

L'article suivant "PDMS-based microfluidics for proteomic analysis", accepté pour publication dans le journal "The Analyst" présente un dispositif microfluidique en PDMS pour l'analyse de protéines. Ce dispositif comporte plusieurs étapes de traitement intégré dans le microsystème, dont une étape de séparation, de sélection et de digestion de protéines avant analyse sur un spectromètre de masse. En tout, l'analyse dure moins de 30 min, à comparer aux 4 heures nécessaires avec les méthodes habituelles.

PDMS–based microfluidics for proteomic analysis

Arash DODGE[*], Edouard BRUNET[*], Suelin CHEN[*], Jacques GOULPEAU[*], Valérie LABAS[**], Joelle VINH[**], Patrick TABELING[*]

[*] *Microfluidics, MEMS and Nanostructures laboratory, ESPCI, 10 rue Vauquelin, 75231 Paris, France*
[**] *Neurobiology and cellular diversity laboratory, ESPCI, 10 rue Vauquelin, 75231 Paris, France*

Receipt/Acceptance Data
Publication data **[]**
DOI: 10.1039/b000000x []

A microfluidic poly(dimethylsiloxane) (PDMS) microdevice was realized, combining on-line protein electrophoretic separation, selection, and digestion of a protein of interest for identification by mass spectrometry. The system includes eight integrated valves and one micropump dedicated to control the flow operations. Myoglobin was successfully isolated from bovine serum albumin (BSA), then selected using integrated valves and digested in a rotary micromixer. Proteolytic peptides were recovered from the micromixer for protein identification. Total analysis from sample injection to protein identification is performed under 30 minutes, with samples of tens of nl. The paper shows that PDMS technology can be successfully used for integrating complex preparation protocols of proteic samples prior to MS analysis.

1 - Introduction

Mass spectrometry has become over the last decade, a major analytical tool for the characterization of proteic samples. The main reason lies in the development of soft ionization modes compatible with macrobiomolecules. Sensitivity and accuracy of the latest configurations coupled to the increasing size of sequence databanks (either proteic or genomic) allow for identifying the proteins present in biological samples in a reliable way. Bottom-up proteomic studies nonetheless requires proteic samples to be subjected to sequences of analytical processes, including purification, separation, reduction/alkylation and enzymatic digestion, followed by desalting, and preconcentration of the resulting peptidic products prior to being injected into the mass spectrometer. Several issues have been raised concerning the preparation process. With non-miniaturized systems, the preparation time is typically hours or days (which may be considered as long for applications requiring high throughput experiments), the sample volume lies in the microliter range (which imposes high dilution ratios for minor proteins) and the transfer of the sample from one step of the protocol to the next is a source of material loss and contamination. In this context it is advantageous to work with a miniaturized and integrated device since this allows to reduce the material consumption, decrease the time response, and, if the surface properties and the architecture of the chip are dedicated, reduce material loss and contamination. These advantages have been highlighted by a number of groups over the last few years. This gave rise to the realization of novel and ingenious lab-on-a-chip (4-10). To summarize a situation that now includes a substantial number of different devices and viewpoints one may say that the goal of these studies is to integrate as many preparation steps as possible and couple them as closely as possible to the ion source of the mass spectrometer. None of them at the moment integrates entire preparation processes, but they succeed to integrate appreciable parts of them. A few examples are given in Refs 1-8 which covers the period 1997-2005.

In this area, the question of the material is crucial. Thus far, microfluidic chips dedicated to proteomic analysis have been elaborated in glass or silicon so as to operate with controlled surface properties, and thus more easily implement established chromatographic techniques. PDMS (PolyDimethylSiloxane) is not currently considered because of its poorly controlled surface properties; in particular, if left untreated, it develops unpredictable surface potentials and, perhaps more importantly, tend to adsorb proteins which obviously contributes to enhance material losses. Different attempts of coating PDMS surfaces are presently undertaken (8-10), but at the moment, the problem of the compatibility of these approaches with the constraints imposed by proteomic analysis has not yet been addressed. On the other hand, PDMS is at the moment the easiest material to actuate (11-13), and thus it may be suitable for integrating complex preparation processes on-chip.

In the present work, we offer an example (we believe to be the first) of a PDMS chip dedicated to proteic sample preparation, and offer the conclusion that this material may be seriously considered for proteomic studies. More specifically, we demonstrate here a microdevice (still non optimized from the proteomic viewpoint) which performs separation of proteins using electro-osmotically driven flow, followed by trapping of the protein of interest using integrated mechanical valves, and enzymatic digestion in a mechanically actuated micromixer. The enzyme is activated on chip in order to minimize autolysis. The resulting peptides are washed out from the chip either directly onto a MALDI target for MS analysis, with or without a desalting step on C18 microcolums. Total analysis time from sample injection into the chip to final

† Electronic Supplementary Information (ESI) available: [details of any supplementary information available should be included here]. See http://www.rsc.org/suppdata/xx/b0/b000000x/

* xxxx@aaa.bbb.ccc

analysis by MS is under thirty minutes and the sample volume lies in the ten nl range.

2- EXPERIMENTAL

Chip layout and operation

The chip is made of polydimethylsiloxane (PDMS) using multilayer soft lithography technology (MSL) (11). Valve actuation channels (in red on Figure 1) are filled with water prior to use in order to avoid air penetrating in the fluidic channels (in green) through the PDMS membranes during operation. A minimum pressure of one bar is applied to the valve actuation channels in order to achieve complete pinching of the fluidic channels. The pressure applied to the pump actuation channels was chosen so as to achieve substantial flow rates (13). The device comprises a protein separation stage, a protein trap and a circular micromixer for protein digestion (Figure 1). An additional feature activates the enzyme directly on chip in order to avoid autolysis prior to the digestion phase. The separation stage consists in a now classic injection/separation device comprising a double-T injection module (14, 15) with an injected sample volume of 1 nL. This part of the chip is solely operated using electrokinetic pumping via electrodes connected to a high-voltage power supply. The trapping module and the circular micromixer digestion module are both mechanically driven using integrated pumps and valves (numbered from 1 to 6 on Figure 1) (13).

Figure 2 describes the device operation cycle. The enzyme is initially pipetted into a reservoir in an acidic medium at pH 2 which keeps it inactive. Valve 6 is then opened and the integrated pump is activated, delivering flow rates of up to 1 µL/min. This will draw the enzyme alongside a flow of basic medium at pH 9, bringing it to an average working pH of 7.5. Valve 1 is then opened and valve 2 is closed while the protein sample is injected in the double-T and then separated using electro-osmotic pumping. The protein sample is separated along the separation channel and when the protein of interest arrives at the trapping zone, valve 1 closes and valve 2 opens, thus capturing it in the 10 nL trapping zone. The trapping zone is larger than the initial sample injection volume in order to compensate for dispersion occurring during separation and thus to capture a maximum of protein molecules of interest.

Valves 1, 3, 4, 5 and 6 are closed at this stage, defining a closed loop thus confining the now active enzyme with the trapped protein in the rotary micromixing module. By activating the pump, one mixes the trapped protein with the activated enzyme and digestion is performed. At the end of the digestion, valves 3 and 4 are opened and an external pressure driven flow at 0.2 bar applied with an electronic pressure controller (Radiospares, France), pumps an elution buffer through the reactor to the outlet of the device releasing a maximum of peptides from the micromixing module. The eluted peptides are either recuperated in an Eppendorf tube for further desalting using ZipTip post processing, either directly spotted onto a MALDI target, either way via PEEK tubing (Upchurch, France) and crystallized by adding 1 µL of 2-5 dihydroxybenzoic acid (DHB) matrix and let to evaporate. The micromixer is regenerated by closing valve 4, opening valve 5 and pushing a regeneration buffer via pressure driven flow at 0.2 bar.

Chip fabrication

The device was microfabricated using MSL (11) in a PDMS-glass device. The fluidic channels and the actuation channels were made using molds fabricated with respectively Shipley 5740 photoresist, and SU8 2015 photoresist (ChimieTechServices, Antony, France). SU8 resist was spincoated on a 2 mm thick four inch in diameter silicon wafer at 1500 rpm to obtain feature mold heights of 23 µm. Shipley resist was spincoated at 1000 rpm obtaining mold heights of 20 µm and further heated at 120 °C during 20 min to obtain a curved geometry (13) with feature heights of 25 µm. Both molds were silanized for 1h with hexamethyldisilazane prior to use in order to facilitate peeling of the PDMS device from its mold. 1:10 curer to PDMS proportioned Sylgard 184 (Arrow electronique, Rungis, France) was spincoated onto the fluidic channel mold at 1300 rpm in order to obtain a 40 µm thick layer, the membrane thickness hence being of 15 µm. 1:10 PDMS was directly poured onto the actuation channel mold obtaining a 5 mm thick device. Both molds are heated in an oven at 75 °C for 40 min. The thicker layer is then unmolded and holes are bored through it using G23 luer stubs (Becton Dickinson, USA) for access to the actuation channels. The thin layer which is still on the mold and the bored thick layer are put in a plasma oxygen oven (Harrick, Ossining, USA) with exposure to plasma during 30 sec at a vacuum pressure of 0.2 torr. The fluidic channels are aligned with the actuation channels and put in contact with one another, thereby creating a permanent seal between the thin and the thick layer. The sealing is further enhanced by heating the layers in an oven for 1 h at 75 °C. The device is peeled off the mold and holes are bored into the device using G23 luer stubs for access to the fluidic channels. The device is again submitted to a plasma ozone treatment during 30 sec with a double-side-polished four inch in diameter 500 µm thick glass wafer (Ediver, Rebais, France), put in contact with the glass wafer and further heated overnight at 75°C to create a permanent seal between the glass and the PDMS.

Instrumentation

A DMIRB epi-fluorescence microscope (Leica, France) coupled to a 4019-5000 CCD camera (Cohu, USA) and a H8568 photomultiplier (Hamamatsu, Japan) was used for the different fluorescence observations and signal detection. A home-made power supply with controllable electrodes was used for applying high-voltages at the reservoirs for electro-osmotic pumping during the sample injection/separation step. A home-made electronic circuit was used for controlling electromagnetic LHDA0533115H valves (The Lee Company, USA) which activate the pressure driving the actuation channels. Tygon tubing (Fisher Labosi, France) was used for connecting the electromagnetic valves to the actuation channels via G23 metallic rods (Phymep, France) that were inserted in the actuation access channel holes for connecting the device to the tygon tubing. This connections scheme can hold up to 4 bar when the holes are properly bored in the PDMS device. PEEK tubing (Upchurch, Cluzeau, France) was used to bring the elution buffer and the regeneration buffer to the device, and also at the peptide outlet of the device. Labview software (National Instruments, France) was used for controlling the system and for data acquisition.

Reagents and solutions

This journal © Royal Society of Chemistry

Myoglobin and lysozyme (Sigma, France) were each separately labeled with fluorescein isothiocyanate (FITC) (Sigma France) by diluting 1mg of FITC in 100 µL of acetone (Prolabo VWR, France), diluting 8.5 mg of myoglobin or 10 mg of lysozyme in 900 µL of 25 mM TRIS buffer (pH 9), adding the FITC in acetone solution to the protein solution and letting incubate for 24h in an Eppendorf tube under constant mechanical mixing motion. TRIS buffer was obtained by adding TRIS powder (Serva, USA) to MilliQ water (Millipore, Bedford, USA), obtaining a final buffer pH of 9. Elution of the peptides from the chip was performed with a 10 mM TRIS, 15% acetonitrile buffer (pH 9.0). FITC-BSA was purchased from Sigma. SDS (Sigma, France) was added to the labeled protein solutions. 50 mM bicarbonate (Sigma, France) buffer (pH 9) was used to activate the trypsin and to regenerate the rotary microreactor after elution of the peptides from the chamber. Trypsin (unmodified bovine trypsin) was purchased from Roche (Mannheim, Germany).

MS analysis

Myoglobin and BSA tryptic digests were dried and resuspended in 10 µl formic acid 1%, desalted using ZipTip C_{18} (Millipore) and eluted with 50% and 80% acetonitrile (HPLC grade, Baker, Deventer, Holland). The desalted peptide mixture was dried and dissolved in 2 or 3 µL of 1% (v/v) aqueous formic acid (Prolabo, VWR, France). The matrix used was a satured solution of 2-5 dihydroxybenzoic acid (DHB, Sigma) in aqueous trifluoroacetic acid (TFA, protein sequencer grade, Applied Biosystems, USA) 0.1%. The sample and the matrix (1:1, (v/v) for myoglobin digestion at r.t., 3:1 (v/v) for myoglobin digestion at 40°C) were loaded on the target and let to dry at atmospheric pressure using the dried droplet method.

Lysozyme peptides were spotted directly onto a stainless steel MALDI target from the chip without desalting, adding 0.5 µL of saturated DHB solution in aqueous TFA/acetonitrile 9:1 (v/v) and prepared using the dried droplet method.

Reduced and alkylated BSA digests were dried and resuspended in 10 µl aqueous formic acid 1%, desalted using ZipTip C18 (Millipore) and eluted with 1.5 µL of water/acetonitrile 2:8 (v/v) directly on the sample plate. 0.5 µL of DHB matrix were added using the dried droplet method.

MALDI-TOF spectra of the peptides were obtained with a Voyager-DE STR Biospectrometry Workstation mass spectrometer (Applied Biosystems Inc., Framingham, USA). The analyses were performed in positive ion reflector mode, with an accelerating voltage of 20 kV, a delayed extraction of 220 ns. Around 1000 scans were averaged. Spectra were calibrated internally using trypsin autoproteolysis products and processed with the Data Explorer software (PE Biosystems). Data mining was performed using ProFound software. A mass deviation of 55 ppm was allowed in the database searches in the NCBInr database bank.

Conditions for database search: mammalian taxonomy, up to 2 misscleavages, tryptic digest with oxidized methionine as variable modification, monoprotonated monoisotopic masses.

RESULTS AND DISCUSSION

Chip operation

By focusing the photomultiplier (PM) over the trapping region, one can monitor and characterize proper functioning of the device (Figure 3). A 1 mM sample of fluorescein in 25 mM TRIS buffer with 5 mM SDS (pH 9) was injected in the double-T for plug formation followed by migration along the separation channel via electro-osmotic pumping. From the migration time t_m, the applied electrical field E, the detection separation length L_{det}, and the electrophoretic mobility of fluorescein (μ_{ep}fluo = $-3.3\cdot10^{-4}$ cm^2/Vs) the electro-osmotic mobility of the buffer in the PDMS channel was determined being $\mu_{EOF} = 6.2\cdot10^{-4}$ cm^2/Vs ($\mu_{EOF} = L_{det}/t_m E - \mu_{ep}$fluo). As studied by Badal et al.(16), electro-osmotic mobility in a PDMS channel can be tuned by varying the concentration of SDS in solution (0.005 – 0.1 % (w/v)). Figure 3 shows that when the injected plug arrives at the detection region via electro-osmotic pumping, the PM signal increases. The protein trap closes and the pump is activated which creates a rapid drop of signal. The mix becomes uniform in under 60 seconds with a dilution factor of 10, corresponding well to the dilution ratio between the micromixer size (100 nL) and the trapping zone (10 nL). The elution buffer is then pumped through the reactor and the signal drops. Figure 3 shows that three cycles performed one after another are reproducible.

Separations

Proteins are known to stick to PDMS surfaces (16-19). In order to perform separations with reduced loss of material, either coating strategies have been developed or the usage of surfactants was tested (17). In this contribution we have used an approach similar as the one described by Badal et al. (16), Homspech et al (20), Roman et al (21). We use SDS in the separation channel so as to create negatively charged assemblies with the proteins. In this context, the separation of proteins can be considered as based on size differences. We worked close to the critical micellar concentration (CMC), which ranges between 6-8 mM corresponding roughly to 0.2% (w:v),. After separation is achieved and the proteins are transported along the separation channel, we capture them and apply a ten-fold dilution in the micromixer, so as to lower SDS concentrations and then comfortably work in conditions where the micellar organisation is disrupted and trypsin digestion is efficient. From the view point of trypsin activity, the dilution is not necessary here since trypsin is considered to remain active even with 1% (w:v) SDS concentration. Dilution could be drastically reduced by reducing the size of the rotary micromixer or piling up several plugs in the micromixer before proceeding to enzyme digestion.

Figure 4a shows the electropherogram of lysozyme, with one major peak (theoretical plate number of 90). Tailing suggests that non-specific interaction occurs with the PDMS surface. Fluorescence microcopy shows that fluorescent lysozyme covers the entire PDMS surface of the injection channels. Moreover after two successive injection/separation runs, no peak can be detected anymore. This suggests that the addition of SDS at 5 mM is not sufficient to prevent sticking to channel walls for proteins with a positive apparent charge.

Figure 4b shows a separation of FITC from FITC-labelled myoglobin and FITC-BSA. Peak appearance times standard deviations are under 0.5% for all three peaks, with theoretical plate numbers of 2400, 900 and 5300 respectively. It is known that SDS coats the PDMS surface resulting in a negatively charged wall (see Ref (21) for instance); in our case, this process, by stabilizing EOF, probably improves the reproducibility of the measurements.
Separations were performed with an electric field of 600 V/cm. The different electrophoretic mobilities measured within the device are for lysozyme $\mu_{Lyz} = 1.1 \cdot 10^{-4} \pm 0.1 \cdot 10^{-4}$ cm^2/Vs, for myoglobin $\mu_{Myo} = -2.6 \cdot 10^{-4} \pm 0.1 \cdot 10^{-4}$ cm^2/Vs and for BSA $\mu_{BSA} = -3.4 \cdot 10^{-4} \pm 0.1 \cdot 10^{-4}$ cm^2/Vs. The major difference between lysozyme from one hand and myoglobin and BSA on the other hand relies in the positive charge of the experimental mobility for lysozyme.

Digestion

Different contaminants have been observed in the preliminary study. The first series of contaminants come from the elution buffer attacking tygon polymer tubing which had been used in preliminary experiments. This has been replaced with PEEK tubing. The most surprising is that the PDMS itself has a very specific and reproducible contaminant desorbing from the walls, its ionization competes with the peptides desorption/ionization process. We believe that this is related to the fabrication of the PDMS when mixing the curer to the polymer, and the stochiometric equilibrium is not well respected.
Figure 5 A shows the MALDI spectrum of the result of a digestion of 1 nL of 10 mg/mL [700 µM] lysozyme solution digested in the 100 nL rotary microreactor for 15 min at 40°C. Heat was applied to the device via a hotplate. Protein identification is unambiguous with a 57% peptide sequence coverage without any alkylation/reduction step of the protein prior to the digestion step. According to the concentration of material we used, no further treatment nor reconcentration was required prior to MALDI-TOF analysis. To prevent peptides to stick to the PDMS walls, the recovery of the peptides from the chip were performed with a buffer containing acetonitrile. When no organic solvent is used to recover the digest, peptides are continuously and unspecifically released from the surface. This was observed using a continuous flush of the sample from the chip onto four different spots of 1 µL on the MALDI target. Peptides were detected in all the spots, showing that they are continuously eluted from the surface and did not come only from the reactor volume which is of only 100 nL. This yields to a large dilution factor of the sample.
Figure 5B shows the result of a myoglobin [8.5 mg/mL = 470 µM] digest performed during 5 min at room temperature. Sample was directly injected into the device along the separation channel via electro-osmotic pumping, therefore resulting in 4.7 pmol of material at the trapping module. Myoglobin identification was unambiguous with 23% sequence coverage, although the digestion was run without any heating at all. This suggests that there are opportunities for optimizing different digestion times and temperatures for different proteins with such a microsystem. Figure 5C shows a digestion performed with a trapped plug of myoglobin [4.2 mg/mL = 240 µM] after it has been separated from BSA [3.3 mg/mL = 49 µM] in the chip. The digestion has been performed in 10 min at 40°C min. There is only a maximum of 240 fmol of material arriving at the micromixer which is the initial amount of sample injected in the double-T. Myoglobin identification is unambiguous with 40 % sequence coverage. A new separation for trapping the BSA plug did not yield to any identification, which shows that for such a protein (BSA contains 17 intramolecular disulfide bridges) the reduction/alkylation step is compulsory. By pretreating BSA via alkylation and reduction prior to injection into the device, it was possible to positively identify BSA, the initial amount of sample injected into the device only being 49 fmol. The signal of the obtained MALDI spectrum (result not shown) nevertheless remains very low which makes it difficult to detect such small amounts of sample injected into the device after a whole operation cycle, this due to peptide sticking to the walls during digestion. Also, in order to improve the signal over noise ratio, we post processed the result of the digestion so as to remove traces of salt, SDS or polymer contamination which tend to increase the noise level. This could eventually be integrated in the future using on chip solid-phase extraction.

CONCLUSION

This is to our knowledge the first PDMS-based microdevice integrating separation, selection and digestion of proteins prior to MALDI-TOF analysis for protein recognition of peptides. It essentially integrates different pumping mechanisms onto the same system (electro-osmosis, pressure-driven flow and integrated actuated pumping), which are decoupled and adapted to each function.
In its present state, our lab on a chip is not optimized from the strict proteomic view-point : there is loss of material due to the double Te geometry of the injector and adsorption to the PDMS walls. We reduced adsorption in the separation unit by adding SDS above the CMC but still there is room for optimization. For real samples, a pre-concentration unit would certainly be required. Also, multiple protein trapping along the separation channel would favor higher throughput. Alkylation and reduction steps of the protein prior to separation would also improve the digestion yields and therefore could be valuable to be integrated on chip. A similar remark holds for salt and SDS removal we performed out of the chip.. All such modifications are certainly worth being considered for improving the device performances.
The lab-on-a-chip that we described here managed to integrate an appreciable part of a complex biological protocol dedicated to the preparation of proteic samples. This may suggest that there is a pathway towards the integration of entire biological protocols if materials well adapted to the integration of actuators. – such as PDMS - are selected..

ACKNOWLEDGEMENTS

The authors wish to thank Jan Lichtenberg from the ETH Zurich in Switzerland for kindly giving us the information to produce a computer-controlled high-voltage power supply and Jean-Baptiste Salmon for helpful discussions. They also wish to thank the CNRS, the ESPCI for funding.

Notes and references

1 Xue, Q.; Foret, F.; Dunayevskiy, Y. M.; Zavracky, P. M.; McGruer, N. E.; Karger, B. L. *Analytical Chemistry* 1997, **69**, 426-430.
2 Ekström, S.; Önnerfjord, P.; Nilsson, J.; Bengtsson, M.; Laurell, T.; Marko-Varga, G. *Analytical Chemistry* 2000, **72**, 286-293.
3 Gao, J.; Xu, J.; Locascio, L. E.; Lee, C. S. *Analytical Chemistry* 2001, *73*, 2648-2655.
4 Gottschlich, N.; Culbertson, C. T.; McKnight, T. E.; Jacobson, S. C.; Ramsey, J. M. *Journal of Chromatography B* 2000, **745**, 243-249.
5 Jin, L. J.; Ferrance, J.; Sanders, J. C.; Landers, J. P. *Lab on a Chip* 2003, **3**, 11-18.
6 Peterson, D. S.; Rohr, T.; Svec, F.; Fréchet, J. M. J. *Analytical Chemistry* 2003, **75**, 5328-5335.
7 Wang, C.; Oleschuk, R.; Ouchen, F.; Li, J.; Thibault, P.; Harrison, D. J. *Rapid Communications in Mass Spectrometry* 2000, **14**, 1377-1383.
8 H.Makamba, J. H.Kim, K. Lim, N. Park, J-H. Hahn, Electrophoresis 2003, **24**, 3607
9 Hillborg H., Ankner J.F., Gedde U.W., Smith G.D, Yasuda H.K., Wilström K., Polymer, 2000, **41**, 6851
10 Ginn B.T., Steinbock O., Langmuir, 2003, 19, 8117
11 Unger, M. A.; Chou, H.-P.; Thorsen, T.; Scherer, A.; Quake, S. R. *Science* 2000, **288,** 113
12 P. Tabeling, *Introduction to Microfluidics*, Oxford Univ Press, 2005.
13 Goulpeau, J.; Tabeling, P.; Ajdari, A. *Applied Physics Letters* 2005, **97**, 1
14 Manz, A.; Harrison, D. J.; Verpoorte, E.; Fettinger, J. C.; Paulus, A.; Lüdi, H.; Widmer, H. M. *Journal of Chromatography* 1992, **593**, 253-258.
15 Effenhauser, C. S.; Manz, A.; Widmer, H. M. *Analytical Chemistry* 1993, **65,** 2637-2642.
16 Badal, M. Y.; Wong, M.; Chiem, N.; Salimi-Moosavi, H.; Harrison, D. J. *Journal of Chromatography A* 2002, **947**, 277-286.
17 James, C.; Davis, R.; Kam, L.; Craighead, H.; Isaacson, M.; Turner, J. *Langmuir* 1998, **14**, 741-749.
18 Linder, V.; Verpoorte, E.; de Rooij, N. F.; Sigrist, H.; Thormann, W. *Electrophoresis* 2002, **23,** 740-749.
19 Sapsford, K. E.; Ligler, F. S. *Biosensors and Bioelectronics* 2004, **19**, 1045-1055.
20 R.W.Homspech, C.D.Garcia, D.J.Henry , D.J.Weiss, J.M.Vivanco, C.S.Henry, The analyst, 2005, **130**, 694-700
21 G.T.Roman, K. McDaniel, C.T.Culbertson, The Analyst, 2006, **131**, 194- 201.

Figure 1

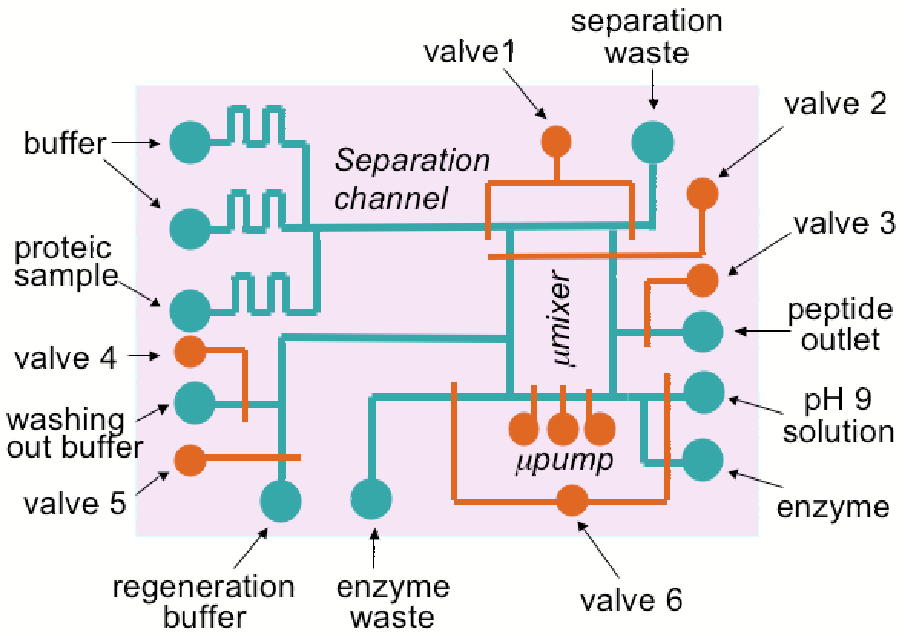

Fig 1 . Sketch of the device. It comprises four modules: an injection/separation module in which pumping is entirely electro-osmotically driven; a protein trapping module; a circular micromixer where pumping is mechanically achieved; an enzyme activation module. Fluidic channels are in blue, actuation channels are in red. Valve actuation channels are filled with water in order to avoid air entering in the fluidic channels through the PDMS membranes. Integrated valves are numbered from 1 to 6. Total microdevice outer dimensions size: 6.4cm x 7.8cm.

.

This journal © Royal Society of Chemistry

Figure 2

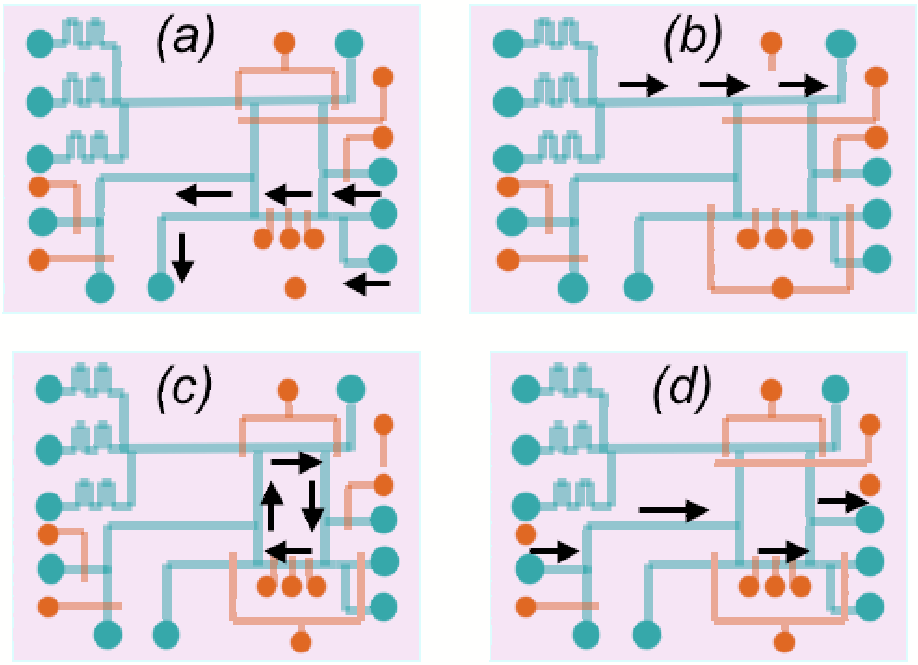

Fig.2 . Chip operation. : (a) The enzyme is activated in the device by being pumped alongside a flow of pH 9 buffer which brings the Trypsine from pH 2 to pH 7.5 in a few tens of seconds (i.e after diffusive mixing is achieved). (b) The protein sample is transported and separated by elecrophoresis and electro-osmotic pumping. Once the protein of interest arrives at the trapping zone, voltage is switched off and two mechanically actuated valves are closed thus confining the sampled protein between them (c) The integrated pump is activated, hence mixing the enzyme with the protein and performing digestion. (d) The pump is stopped and a pressure is applied to an inlet of the chip thus washing out the resulting peptides either into an eppendorf tube for further ZipTip postprocessing, or directly onto a MALDI target for analysis

Figure 3

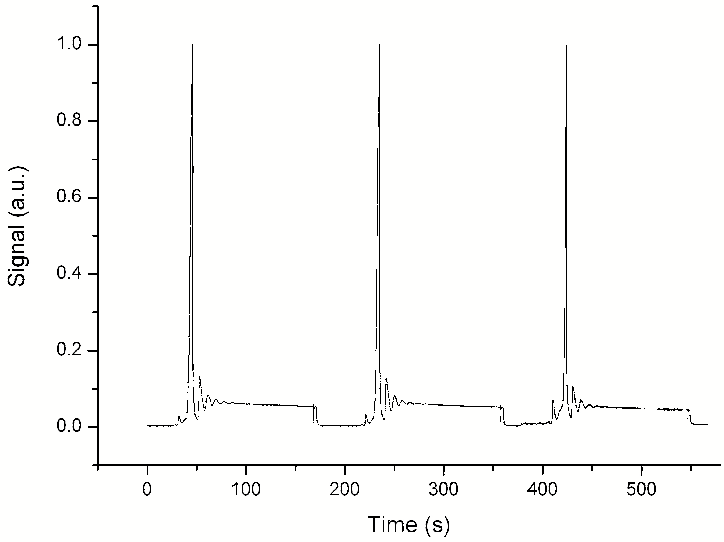

Fig 3 : Operation cycles visualized at the protein trapping region performed with 1 mM fluorescein solution in 25 mM TRIS buffer (pH 9). First the injected plug arrives in the detection zone which leads to a strong increase in signal. Pumping is switched from electro-osmotically driven flow to mechanical pumping via the integrated valves and pump thereby inducing mixing. The signal oscillates as the plug passes by the detection region at each cycle, being diluted at each turn until the solution is uniform, inducing signal stabilization. Finally the mix is eluted from the microreactor using external pressure applied to a reservoir of elution buffer.

This journal © Royal Society of Chemistry

Figure 4

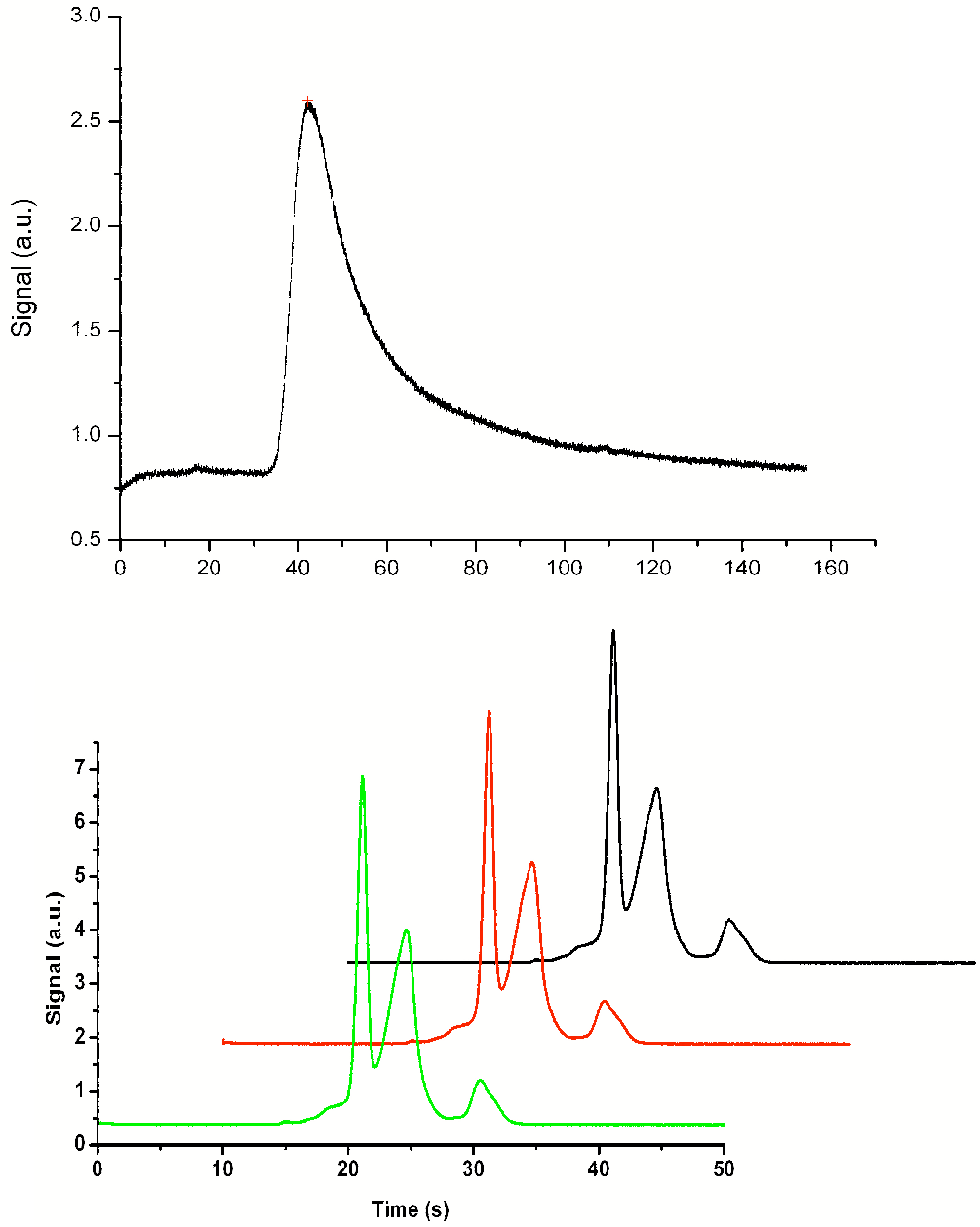

Fig. 4: (A) Lysozyme-FITC peak [1 mg/mL] in a 25 mM TRIS, 5mM SDS buffer. (B) FITC [1 μM], Myoglobin-FITC [235 μM] and BSA-FITC [49 μM] in a 25 mM TRIS, 5 mM SDS buffer (pH 9). All separations are performed at 600 kV/cm.

Figure 5

(A)

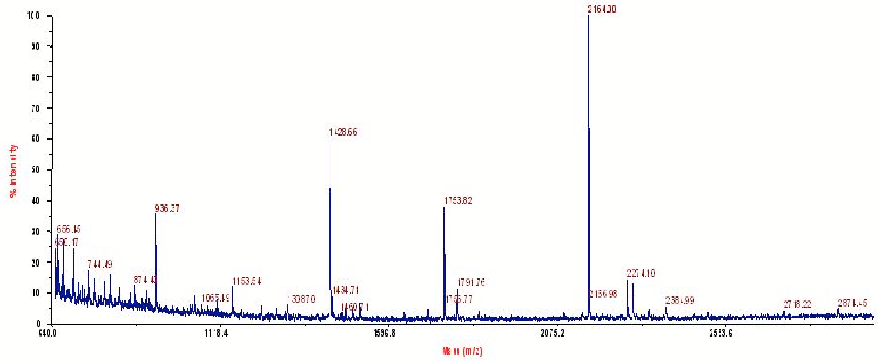

(B)

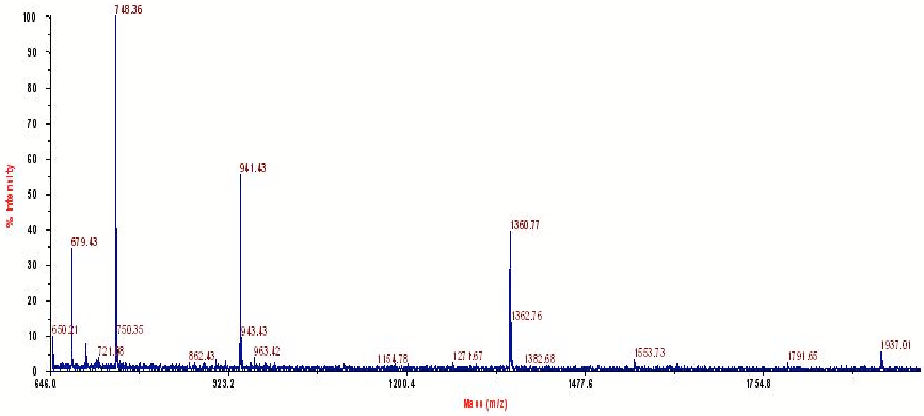

(C)

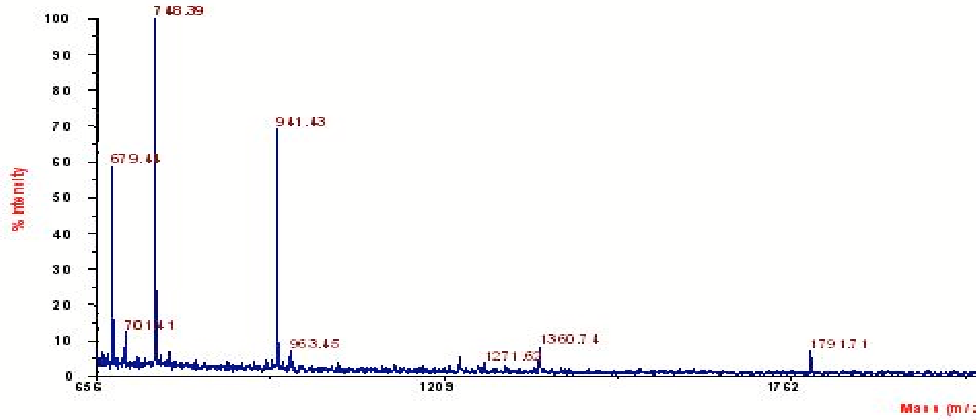
748.39
941.43
679.44
701.41
963.45
1360.74
1271.65
1791.71
% Intensity

Fig. 5: (A) Tryptic digest of 1nL Lysozyme sample [10 mg/mL] in the 100 nL rotary reactor. Digestion performed during 15 min at 40°C. Peptide coverage is of 57%, recognition probability is of 100%. Protein was directly spotted onto MALDI target. (B) Tryptic digest of 10 nL Myoglobin-FITC sample [8.5 mg/mL] in the 100 nL rotary reactor. Digestion performed during 5 min at ambient temperature. Peptide coverage is of 27%, recognition probability is of 100%. Initial injected amount of sample 4.7 pmol. (C) 1nL Myoglobin-FITC sample [4.2 mg/mL] after separation from BSA-FITC [5 mg/mL] in the 100 nL rotary reactor. Digestion performed during 10 min at 40°C. Peptide coverage is of 27%, recognition probability is of 100%. Initial injected amount of sample 230 fmol. Both digests were post-processed using Zip Tip techniques.

Annexe B

Article sur le gradient de concentration soumis à Lab on a Chip

Cette article soumis au journal "Lab on a Chip" reprend le travail du chapitre 3 sur l'utilisation de la dispersion de Taylor-Aris pour réaliser des gradients de concentration indépendant du coefficient de diffusion des espèces.

Building up longitudinal concentration gradients in shallow microchannels

Jacques Goulpeau*, Barbara Lonetti, Daniel Trouchet, Armand Ajdari, Patrick Tabeling

Théorie et Microfluidique, CNRS-ESPCI UMR 7083
10 rue vauquelin, 75005 Paris, FRANCE,
and
Bertin Technologies,
10bis rue Ampère, 78053 Montigny-le-Bretonneux, FRANCE

* jacques.goulpeau@espci.fr
Tel : +33140795153
Fax : +33140795157

[Insert Running title of <72 characters]

ABSTRACT

We demonstrate a compact and low consuming (60 nL) method dedicated to generate concentration gradients along microchannels with shallow parabolic cross-sections. The regimes of dispersion taking place in such systems and the cocentration field that are produced are described theoretically and experimentally. Experiments are performed in PDMS (Polydimethylsiloxane) microchannels actuated by integrated valves. Detailed comparison between theory and experiment for the "short time" and "long time" regimes leads to excellent agreement. The system is used to successfully set up a series of isolated microchambers with mixtures of increasing solute concentrations. This work may lay the foundations of a novel screening approach.

KEYWORDS: Concentration gradient, Taylor-Aris dispersion, Microchannel, Screening

[Insert Running title of <72 characters]

INTRODUCTION

There is an interest building up controlled concentration gradients in microfluidic systems for a number of different, often unrelated, reasons: in some cases, these concentration gradients are used for the study of micrometric size entities responding to non homogeneous environments (for example a cell in a chemical gradient)[1]. In other situations, concentration gradients produced in a discrete form are used to develop novel screening approaches[2]. At the moment, the number of methods and systems available in the literature for building up concentration gradients in microfluidic systems is modest. Efforts for developing controlled concentration gradients normally to microchannel flows has given rise to studies of general relevance[3-7] and to the fabrication of dedidated devices[8-10]. To the best of our knowledge, the case of concentration gradients developing *along* microfluidic channel streams has not yet been investigated in detail at the experimental level. Such gradients would be interesting to set up on-chip so as to miniaturize techniques currently used in analytical chemistry, or to investigate how entities such as cells respond to a greater variety of patterns of chemical heterogeneities. As will be shown in the present paper, these gradients could also be used for developing novel screening strategies which, compared to existing technologies[11-13] might simplify the scheme of actuation.

On theoretical grounds, the problem of the structure of longitudinal dispersion gradients along channel flows is a classical problem in fluid mechanics. The solution for the simplest geometries has been worked out long ago by Taylor[14] and Aris[15]. More recently, the case of shallow microchannel[16] flows with arbitrary cross-sections was addressed[16, 17]. In the latter reference, it was shown that narrow microchannels with non rectangular cross-sections develop three regimes of longitudinal dispersion (i.e one more than the classical case). The new one – called "short

time" regime - possesses a number of interesting properties: it spans an appreciable range of time and, under certain conditions, the effective dispersion is found independent of the diffusion constant of the solutes introduced in the system. This means that in such a regime, the system builds up a concentration gradient independent of the diffusion coefficients of the species that are dispersed in the system. This regime, which does not require any calibration, appears well adapted to microfluidic applications.

The work we report here is dedicated to build up controlled concentration gradients *along* microchannels of simple geometry, spanning two of the ranges of time singled out by Ref[17]. We will show that the concentration gradient that we set up fits well with the theoretical expectations.

The paper is organized in two parts: in a first part, we describe the theoretical analysis of the concentration field: we extend the work of Ref[17] by deriving a number of useful formula still not published in the literature. In the second part, we describe the experiment and finally, we compare the theory with the experiment. As an outcome of this work, we succeeded to set up a series of isolated microchambers with mixtures of increasing solute concentrations, a system that may lay the foundations of a novel screening approach.

THEORETICAL SECTION

The three regimes of longitudinal dispersion taking place along a microchannel

The geometry of the microchannel we consider, along with the definition of the coordinate axes are shown in Fig 1. Although the calculation can be carried out with arbitrary shallow cross-sections, we will mostly restrict ourselves to shallow parabolic shapes, such as those sketched in Fig 1. This restriction is justified by the geometry that we investigated experimentally (see the next section).

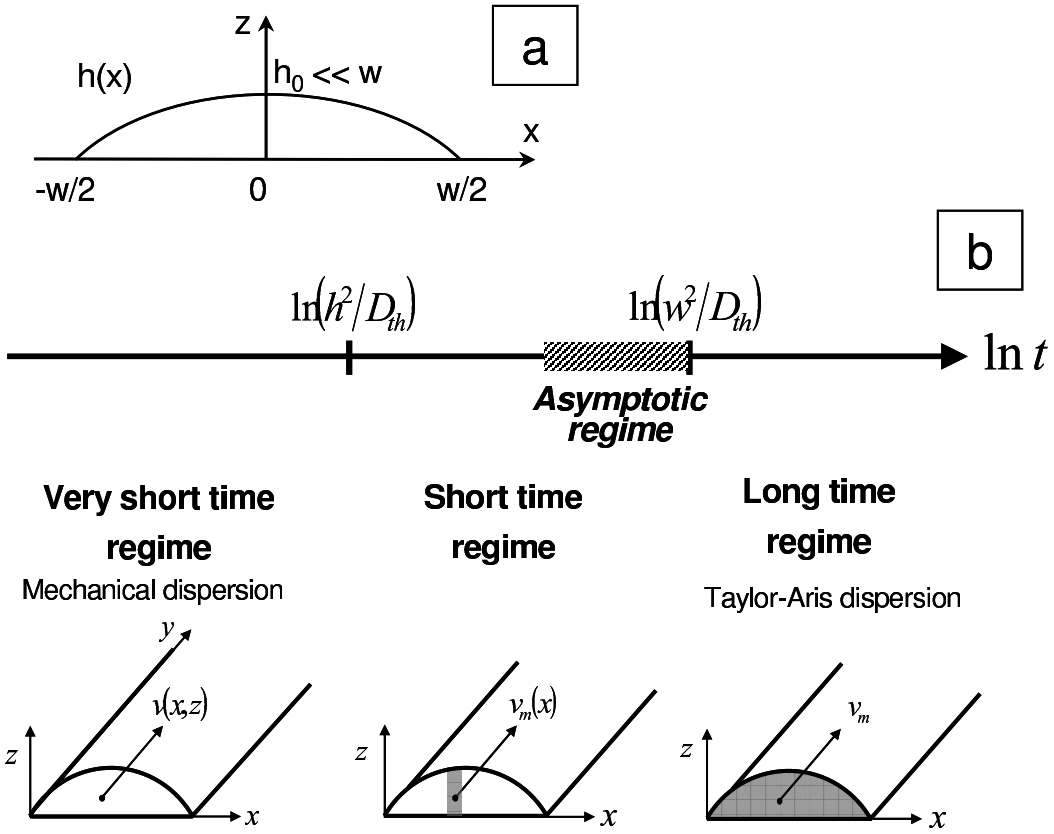

Figure 1: (a) coordinate axes in the cross-sectional plane of the channel - the flow is driven along y-axis-. (b) Description of the three different regime of dispersion plus the asymptotic regime described in the text.

In the systems we are considering here, as shown in Ref[17], there exist three different regimes of dispersion, These regimes are displayed in Fig 1b. We take the same language as in Ref[17].

At "very short" times ($t << h_0^2/D_{th}$, where D_{th} is the diffusion coefficient of the considered species), a regime takes place for which the tracer molecules follow the flow streamlines. This regime is thus controlled by mechanical dispersion. At "short" times, ($h_0^2/D_{th} << t << w^2/D_{th}$), we have an intermediate regime in which the dye is advected at a speed averaged across the

smaller dimension of the channel ; the spreading rate of the dye along the mean flow is controlled by a coupling between Taylor-Aris diffusion and pure advection. At "long times" ($t >> w^2/D_{th}$), we recover the usual Taylor Aris dispersion regime, where the dye mass center is advected at a speed averaged throughout the channel cross-section, while the longitudinal spreading of the spot is controlled by an ordinary Taylor Aris diffusive process in which the width w is the characteristic length scale (see Ref[14, 15]).

In order to facilitate the comparison with the experiment and for completeness, we will derive here analytical expressions for the concentration profiles along the channel (i.e along y and averaged along x) for the three regimes. These formulas have not yet been published in the literature and are not particularly easy to obtain. For the sake of clarity, the expressions of the concentration profiles for the "very short" time regime are listed in appendix; the analysis developed in the main body of the paper is thus concerned with the "short time" and the "long time" regimes of dispersion.

Analysis of the short time regime of dispersion

In this regime, the mass center of a dye blob moves at a mean velocity $v_m(x)$ averaged across the coordinate z (see Fig 1b). In the mass center frame of reference, the dye spreads diffusively along the flow streamlines (i.e along the direction y), and this process is controlled by an effective diffusion coefficient that reads (cf Ref[14, 15]) :

$$D_{eff}(x) = D_{th}\left(1 + \frac{1}{210} Pe_h(x)^2\right) \quad (1)$$

[Insert Running title of <72 characters]

in which $Pe_h(x) = v_m(x)h_0/D_{th}$ is the Péclet number defined at location x. The normalized concentration profile $\rho_l(y)$ can be further found by noting that diffusion along x is negligible within the range of time we are considering. The spread of the dye material elements is thus controlled by advection. Under such conditions, the expression for the x-averaged profile of the dye concentration along *y* reads (its detailed derivation is displayed in appendix).

$$\rho_l(Y,T) = \frac{3}{8}\int_{-1}^{1} H(X)\left(1 + erf\left(\frac{Y - \frac{y_i(X)}{h_0 Pe_h\, T} - H(X)^2}{2\sqrt{Pe_h^{-2} + \frac{1}{210}H(X)^6}}\sqrt{T}\right)\right)dX \tag{2}$$

with $erf(a) = 2/\sqrt{\pi}\int_0^a e^{-\xi^2}d\xi$, $Pe_h = v_m(0)h_0/D_{th}$, $H(X) = h(x)/h_0$ the normalized shape of the channel, $X = 2x/w$, $Y = y/L(t)$ (with $L(t) = 2/3\,v_0 t$, see appendix), $T = D_{th}\,t/h_0^2$ and $y_i(X)$ the initial shape of the interface separating the part of the fluid containing the analyte from the other part free of it. At long times ($T \to \infty$), one obtains the following limiting profile from Eq. 2:

$$\rho_l(Y) = 1 - \frac{3}{2}\sqrt{1-\sqrt{Y}} + \frac{1}{2}\left(\sqrt{1-\sqrt{Y}}\right)^3 \tag{3}$$

We underline here that the profile depends only on Y and on the channel geometry (Eq. 12); i.e on velocity v_0 and time *t*. This expression can be more directly established by noting that it is permissible to neglect the diffusive concentration gradient in the *y* direction. At long times, one thus obtains no explicit influence of the diffusion constant D_{th} on the concentration profile. This

result originates from the fact that diffusion broadens the concentration distribution at a rate slower ($\sqrt{t}$) than mechanical stretching (t). We thus have, for times long compared to h_0^2/D_{th} - but still small against w^2/D_{th}, so as to stay in the short time regime - concentration profiles independent of the diffusion constant D_{th}. We call this subregime "asymptotic" (figure 1b). As a consequence of this property, if a mixture including several reactants is to be spread along shallow parabolic microchannels, the concentration profiles that will be obtained will be the same for all the compounds of the mixture. As announced in the introduction, this property is interesting from a practical viewpoint.

One may further determine more accurately the boundaries of the "short time regime", and within this regime, the practical limits of the domain for which the concentration profile is independant of the diffusion constant, i.e. the "asymptotic" regime. To simplify the picture, one may restrict ourselves to Pe>25, for which the limits that we give below are independant of the Peclet number. By working with the variance of each distribution and for a parabolic cross-section, one obtains that the short time regime holds for $0.043 h_0^2 / D_{th} < t$. Within the short time regime, we find that the range of existence of the asymptotic regime (within which the concentration profile is independant of the diffusion constant of the analyte - with an average absolute error of 3% and a maximum absolute error of 15% on the concentration profiles -) can be defined by the following inequality: $0.5 h_0^2 / D_{th} < t$. These findings are summarized in Table 1. They may be conveniently used for designing gradient generator devices.

[Insert Running title of <72 characters]

Analysis of the "long time regime" of dispersion

We consider here the '"long time" regime, i.e a regime where the tracer has entirely diffused across the cross-section of the main canal (figure 1b). Here, the longitudinal dispersion of the concentration field is governed by an ordinary Taylor-Aris dispersion process that is fully described by an effective diffusion coefficient:

$$D_{eff} = D_{th}\left(1 + \kappa\, Pe_w^2\right) \tag{4}$$

in which $Pe_w = U_m w / D_{th}$ is the Péclet number defined in the width and U_m the mean velocity in the cross section channel. For parabolic cross section κ equal 0.0031[17]. The formula for the concentration gradient is described in the appendix for high Péclet numbers.

Table summarizing the results of the theoretical analysis

For the sake of clarity, we display in Table 1 the regimes of dispersion we calculated for the particular case of parabolic cross-sectional channels. We also indicate the temporal conditions of existence for each regime so as to have a list of results of practical interest. Table 1 is particularly useful to build up longitudinal concentration gradients in micromoulded devices, which bear on a technology well adapted for the fabrication of cross-sectional parabolic microchannels[11] - we will consider an example in the experimental section.

For the asymptotic regime, the temporal conditions of existence can be expressed as conditions on the diffusion coefficient:

$$0.5h_0^2/t \le D_{th} \le 0.035w^2/t \tag{5}$$

[Insert Running title of <72 characters]

Thus within this range of diffusion coefficient, the gradient is independent of diffusion. To illustrate this formula, if one considers an aspect ratio h_0/w of 1/10, one infers that the ratio between the upper and lower time limits is equal to $0.07(w/h_0)^2 = 7$. For smaller aspect ratios (1/30), this ratio is 63. We thus may have, in practical devices, comfortable ranges of existence for the asymptotic regime.

Regime		**Time conditions**	**Characteristic length**	**Remarks**
Very short time		$t < 0.043 h_0^2/D_{th}$	$v_0 t$	Diffusion independent
Short time regime	early times	$0.043 h_0^2/D_{th} < t$ $t < 0.5 h_0^2/D_{th}$	$2/3 v_0 t$	Diffusion dependent
	asymptotic	$0.5 h_0^2/D_{th} < t$ $t < 0.035 w^2/D_{th}$	$2/3 v_0 t$	Diffusion independent
Long time		$0.035 w^2/D_{th} < t$	$16/35 v_0 t$	Diffusion dependent

Table 1: Summary of the main results of the theoretical section for parabolic cross sections. The various time limits are justified in the text. The characteristic lengths L(t) are determined in the text and the appendix.

EXPERIMENTAL SECTION

Description of the experimental set-up

The microfluidic device is sketched in Figure 2a. The fluidic channel is made in PDMS Sylgard 184 (Arrow Electronique, Rungis, France); it is composed of a Y-shaped channel connected to reservoirs filled with, respectively, deionised water (DI) and a buffer containing 1 mM free acid

fluorescein and 10 mM NaOH (n°46955 Sigma-Aldritch, Saint Quentin Fallavier, France) in DI water. The diffusion coefficient of fluorescein is 3 10^{-10} m^2/s[19]. To accurately control the flows, microvalves are integrated on the chip, using Multilayer layer soft lithography technique[11] (MSL). These actuators incorporate membranes that squeeze the working channel when the actuation channel, placed just above it is pressurized. In our case[18], a pressure as low as 0.3 bar is sufficient to completely close the valve. The two independant valves sketched in Fig 2 allow the full control of the flow injection conditions. Additional valves, actuated by a serpentine channel, isolate the main channel into different chambers, located 1mm from each other. The actuation pressure forcing the closure of the valves is switch on or off by using high speed electrovalves LHDA0533115H (LEE Company, Voisin-le-Bretonneux, France) controlled by a LabView program.

Two negative masters patterned by standard photolithography are employed for the working and the actuation channels. The mould for the working channel is made out of the SJR 5740 positive photoresist (CTS, Antony, France). The photoresist is spin coated at 20°C at 1000 rpm for 10s on a 4 in. silicon wafer. After the development, the photoresist is heated above its glass transition temperature, 120°C for 20 min, in order to obtain round shape channels. The mould for the actuation channel is made in SU8-2100 negative photoresist (CTS, Antony, France) spin coated at 2000 rpm for 30 s on a 4 in. silicon wafer. The dimensions of the microchannels are measured with a profilometer. Positive replicas with the working and the actuation layer are fabricated by moulding the PDMS against the master, the two layers being bonded through a gradient concentration of the curing agent in the two layers[11]. A reversible seal is done between a glass cover slide and the PDMS. The actuation channels are 130 µm in the height; two different widths for the working channels are used: 200 µm and 300 µm. The height is 27 µm in all cases.

[Insert Running title of <72 characters]

The flows are hydrostatically driven. Optical observations are made by using a LEICA inverse epifluorescence microscope and the images are taken by using a CCD camera. The images are further digitalized and treated on a computer by using MathLab software. In order to normalized the fluorescence intensity, each experiment starts with measuring the width-averaged fluorescence intensity profiles along the channel in two cases : filled with DI water (background = B) and filled with the buffer including a known quantity of fluorescein (1mM). The fluorescence signal (S) is then normalized using the formula $(S-B)/(M-B)$. By doing this, one removes the non homogeneities induced by the fluorescence excitation source. Depending on the circumstances, the concentration profiles are measured with the serpentine valves left open or after the serpentine valves are closed. In the latter case, we averaged out the signal in each chamber and thus obtain a "frozen" picture of the system.

[Insert Running title of <72 characters]

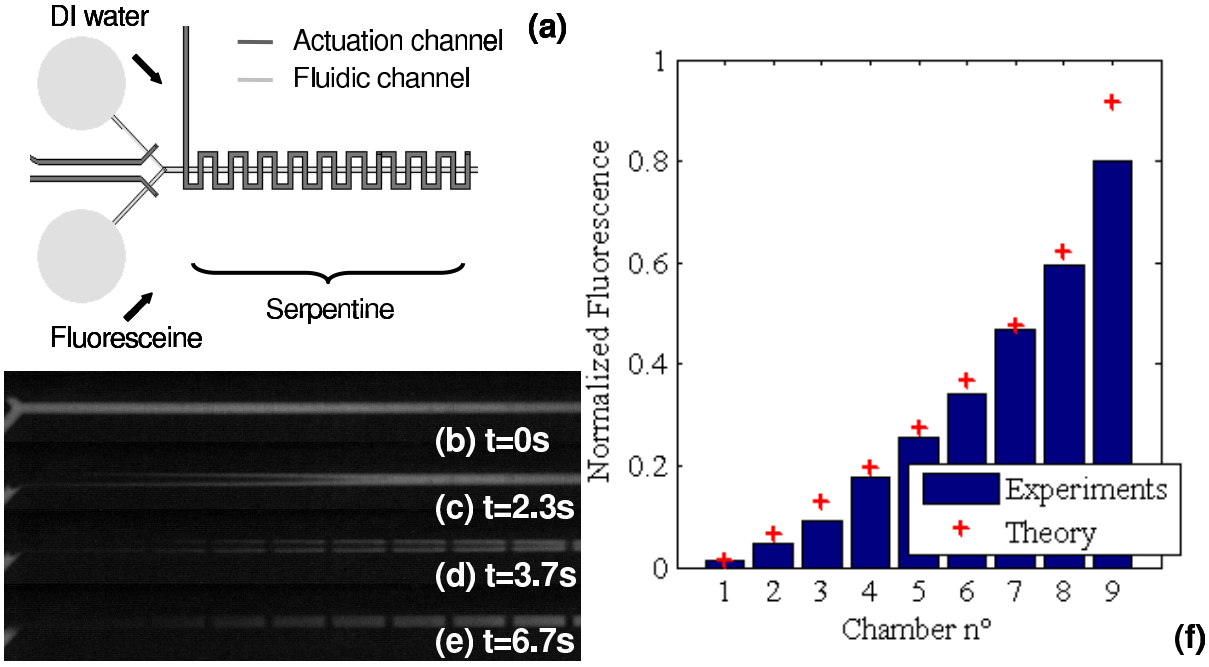

Figure 2: (a) sketch of the device. (b-e) sequence of steps leading to the formation of a longitudinal gradient (f) fluorescein concentration levels measured in the nine different chambers at time t=6.7 s. The crosses represent the theoretical description (Eq. 3). (w = 200 µm, h_0 = 27 µm)

Procedure for building up longitudinal gradients

In order to produce controlled longitudinal gradients of fluorescein concentration along the main channel, one needs to form a sharp initial plug, or, equivalently, one needs to produce a sudden change in the flow conditions. The task is very well accomplished with the valves. The particular sequence we consider here is shown in Fig 2b and c: Initially, the main channel is filled with fluorescein (see Fig 2b). Suddenly, a pulse of DI water is flushed in the solution (by opening the top valve on the left of Figure 2a and closing the lower one); eventually, at t= 3.7 s, the

serpentine is closed (see Fig 2c). Fig 2f shows the content of each chamber 3s after they have been closed. One obtains a stepwise increase of the fluorescein concentration along the main microchannel, spanning a broad range of concentration levels (from 1.5 to 80 %). This demonstration experiment illustrates that the system is suitable for screening the properties of multicomponent systems at different concentration ratios. In view of being able to predict (and therefore control) the concentration field we are building up, we now proceed to a comparison between the experiment and the theory.

Comparison between theory and experiment in the short time regime

In order to compare the theory with the experiment in the short time regime, we restrict ourselves to considering ranges of time comprised between 0.14 and 2.9 s, which, in terms of the dimensionless parameters introduced in Fig 2, represent a range comprised between 0.058 and 1.2 h_0^2/D_{th}. We may check that for this range of time, we do not penetrate the long time regime since the characteristic time $0.035w^2/D_{th}$ = 4.7 s (w=200µm here) is located above the range of time we specifically address here. The set of concentration profiles we could measure in this range of time is shown in Fig. 3b. On the curves, the fluorescence intensity averaged along the x-axis is normalized as explained before so as the absolute maximum of the curves is equal to unity. In Fig. 3b, the gradient profile is measured continuously in time along y. The y-axis is rescaled by the gradient length $L(t) = 2/3 v_0 t$ (table 1) where $2/3 v_0 = 2.9\, mm/s$. In the experiment, a slight dissymmetric initial interface shape is produced. Here, we measure it and took this perturbation into account by using the Eq. 2 of the model with a prescribed non zero y_i. In such conditions, we obtain a remarkable agreement between the theoretical expectation and the experiment (Fig. 3). The small deviations observed at short time (0.14s) are presumably due

to a slightly bent initial interface. The asymptotic regime, as described in the theory is neatly observed in the experiment. One may underline that no fitting parameter is introduced in the comparison.

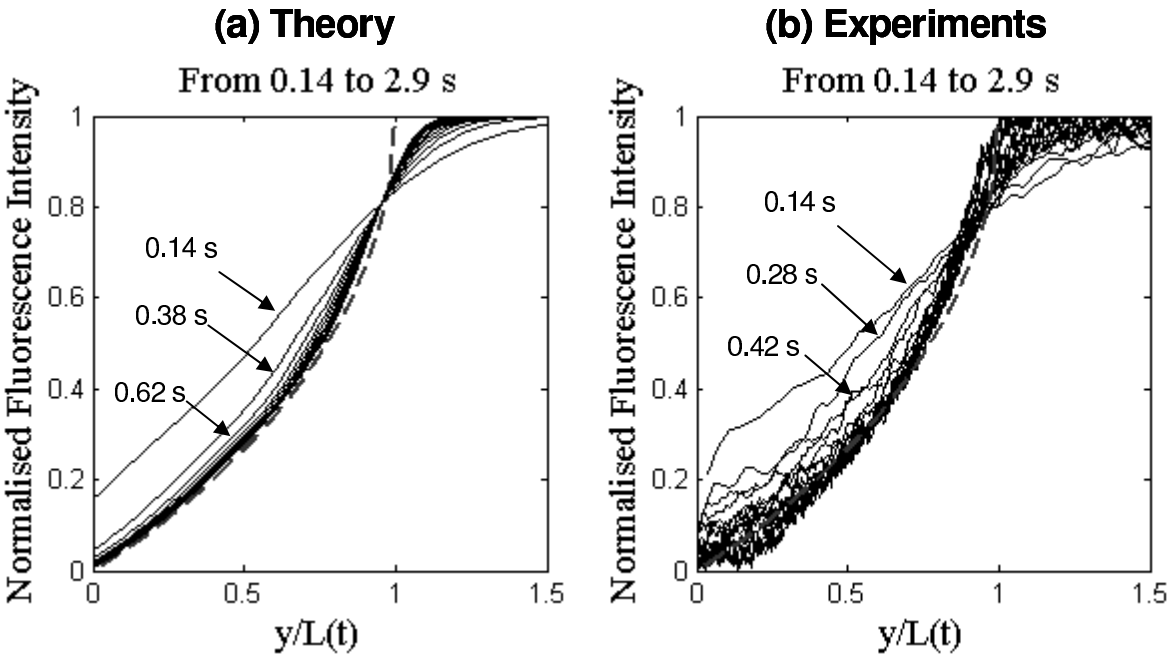

Figure 3: Comparaison between theory (a) and experiments (b). No fitting parameters are used. The diffusion coefficient for fluorescein is taken equal to 3 10^{-10} m^2/s[19]. As times increase, the curves tend to the hybrid regime profile (--).

A similar agreement is obtained with the demonstration experiment of Fig 2f, where the range of time we considered turns out to correspond to the short time regime.

Comparison between theory and experiment in the long time regime

In order to perform a similar analysis in the long time regime, we consider ranges comprised between 13 and 120 seconds, thus representing, in terms of characteristic times w^2/D_{th} domains

comprised between 0.043 and 0.4 (w=300 μm here). We plot the measurements by using dimensionless quantities suggested by Eq. 13 (see the appendix):

$$y^* = \frac{y - y_m}{2\sqrt{D_{eff} t}} \quad (6)$$

where D_{eff} is given by Eq. 4(see the theoretical section). The data to evaluate D_{eff} from Eq. 4 were measured (U_m, w) for each experiment. The centers of the distribution (y_m) were evaluated by fitting each data with a sigmoid function. The results are shown in Fig 4. Here Péclet numbers range from 150 to 460. We obtain that the data collapses onto a single curve, consistently with the theory. Moreover, the theoretical prediction for κ (for the case of a parabolic cross sections , it is 0.0031[17]) is found in good agreement with the experiment. The slight deviation observed between the theoretical curve and the measurement at short time (around 13.3 s = $0.044w^2/D_{th}$) may signal the presence of a gradual transition between the short time regime and the long time regime. In the experiment, we estimate the transition between the two regimes takes place around 0.04 w^2/D_{th} (data not shown) which is in good agreement with the theoretical prediction[17] and our calculation (0.035 w^2/D_{th}).

[Insert Running title of <72 characters]

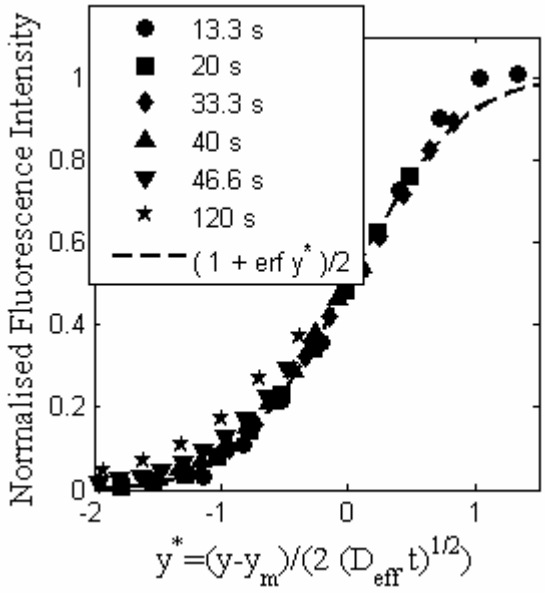

Figure 4: Measurements of concentration gradients in the long time regime for different time and speed (U_m=150µm/s, 460µm/s) plotted with adimensional variables. The theoretical curve (–) is shown.

CONCLUSIONS

In conclusion, a novel method dedicated to setting up concentration gradients along shallow micro-channels was presented. Microchambers with different concentrations can be isolated, allowing screening applications. In a regime called asymptotic regime, the concentration profiles are independant of the diffusion constant of the species spread in the system and thus feeding the microchambers. These profiles depend on the flow velocity and time. The asymptotic regime extends, in some dimensionless units, between a time equal to 1 and several tens, for reasonably shallow microchannels. This regime can thus be conveniently used for screening different analyte concentrations, consuming only minutes amounts of material (60 nL), without any calibration nor a priori knowledge of the diffusion constants of the analytes. Still from a

screening prospective, the number of chambers can be easily increased, and, if necessary, by changing the injection conditions, one may focus on a particular range of concentration conditions. Last but not least, in all cases, a single serpentine actuation channel and two microvalves only are used. This may represent a simplification compared to other strategies for which, unpleasantly, the number of independant valves increases with the number of chambers.

Acknowledgment

We acknowledge Bertin Technologies, ESPCI and CNRS for their support to the present work.

[Insert Running title of <72 characters]

Appendix: Derivation of the formulas in the three different dispersion regimes

In this appendix, we derive the linear concentration profile of a compound along a microchannel in the presence of a flow (figure 2a). We define the mean concentration in a section of the microchannel by the formula:

$$\rho_l(Y,T) = \frac{1}{\int_0^1 H(X)dX} \int_0^1 H(X) \int_0^{H(X)} C(X,Y,Z,T)\, dZ\, dX \qquad (7)$$

With $X = 2x/w$, $Z = z/h_0$, $H(X) = h(x)/h_0$ and $C = c(x,y,z,t)/c_0$. The normalizations for time t and coordinate y will depend on the particular regime we consider. The initial conditions are the following: For t<0, the channel is filled with a solution containing the compound (concentration c_0). At t=0, fresh solution is drawn in, the interface between the two solutions stretches out, which eventually leads to the formation of a concentration gradient along the channel described by function $\rho_l(Y,T)$.

In the approximation of low Reynolds numbers and for low aspect ratio channels (h_0<<w), the main term of the development of the velocity profile for $h/w \to 0$ is given by:

$$V(X,Z) = 4H(X)^2 \frac{Z}{H(X)}\left(1 - \frac{Z}{H(X)}\right) + o(h_0/w) \qquad (8)$$

where $V = v(x,z)/v_0$, $v_0 = -h_0^2/8\eta\, \partial P/\partial y$ being the maximum velocity in the channel.

Very short time regime: for times shorter that the time diffusion across the height ($t << h_0^2/D_{th}$), the interface spreading is mostly due to kinematical dispersion. In this case the y coordinate is

renormalized by using the expression $Y = y/v_0 t$. Although the calculation can be carried out for a channel of arbitrary cross section H(X), we restrict ourselves, for simplicity, to a parabolic cross-sectional channel defined by $H(X)=1-X^2$; in such conditions, the concentration profile is given by:

$$\rho_l(Y) = 1 - \frac{3}{2}\int_{Z_-}^{Z_+} \sqrt{\frac{(Z_+ - Z)(Z - Z_-)}{Z}}\,dZ \tag{9}$$

With $Z_\pm = \left(1 \pm \sqrt{1-Y}\right)/2$.

Short time regime

For times long enough for the concentration to be homogenous in the height but too small for achieving homogeneity in the width ($h_0^2/D_{th} \ll t \ll w^2/D_{th}$), the concentration $C(X,Y,Z)$ is obtained by considering that the material lines are advected at a mean velocity equal to $2/3\, v_0 H(X)^2$ with an effective diffusivity given by the Aris formula $D_{eff}(X) = D_{th}\left(1 + Pe(X)^2/210\right)^{15}$. Here the Péclet number is "local": it is given by the expression $Pe(X) = 2v_0 h_0 H(X)^3/3D_{th}$. Calculations lead to the following result for the concentration field :

$$C(X,Y,T) = 1/2 + 1/2\, erf\left(\sqrt{T}\,\frac{Y - H(X)^2 - y_i/h_0 Pe_h T}{2\sqrt{Pe_h^{-2} + \frac{1}{210}H(X)^6}}\right) \tag{10}$$

with $Pe_h = 2v_0h_0/3D_{th}$, $T = D_{th}\,t/h_0^2$ and $Y = y/h_0Pe_hT$. The length $h_0Pe_hT = 2/3\,v_0t$ represents, geometrically, the extension of the gradient along the stream. y_i is the interface position at t=0. We note that the influence of the initial conditions decreases with time as t^{-1}. As time increases, the concentration profile tends to become independent of the diffusivity constant D as explained in the main text; it tends to be prescribed solely by the channel geometry. We obtain its expression by taking the limit $T \to \infty$ in Eq. 2. We may obtain the same result by neglecting the gradients along y in the advection diffusion equations (this is justifed by noting that mechanical stretching increases faster (t) than Taylor-Aris diffusion ($t^{1/2}$)). By introducing a mean velocity $V_m(X)$ defined by:

$$V_m(X) = \frac{2}{3}H(X)^2 \tag{11}$$

we obtain the following formula for the concentration gradient :

$$\rho_l(Y) = \frac{1}{\int_0^1 H(X)dX} \int_0^{V_m^{-1}(2Y/3)} H(X)dX \tag{12}$$

where V_m^{-1} is the inverse function of Eq. 11. For a parabolic cross-sectional shape, we find Eq. 3.

Long time regime: for times longer than w^2/D_{th}, diffusion is entirely established in the channel cross-section and the classical Taylor formula can be used with an effective diffusion coefficient $D_{eff} \approx \kappa U_m^2 w^2/D_{th}$ [14] for high Péclet number, U_m being the velocity averaged throughout the

[Insert Running title of <72 characters]

channel cross-section. For parabolic thin cross-sections, the coefficient κ has been derived[17]: it is found equal to 0.0031. The concentration function is then described by:

$$\rho_I(Y,T) = 1/2 + 1/2\, erf\left(\frac{Y-1}{2}\sqrt{T}\right) \tag{13}$$

with $T = D_{th}\, t/\kappa w^2$ and $Y = y/U_m\, t$. For parabolic cross-sections one has $U_m = 16/35\, v_0$.

[Insert Running title of <72 characters]

References

(1) Li Jeon, N.; Baskaran, H.; Dertinger, S. K.; Whitesides, G. M.; Van de Water, L.; Toner, M. *Nat Biotechnol* **2002**, *20*, 826-830.

(2) Zheng, B.; Roach, L. S.; Ismagilov, R. F. *J Am Chem Soc* **2003**, *125*, 11170-11171.

(3) Jeon, N. L.; Dertinger, S. K. W.; Chiu, D. T.; Choi, I. S.; Stroock, A. D.; Whitesides, G. M. *Langmuir* **2000**, *16*, 8311-8316.

(4) Jiang, X.; Ng, J. M.; Stroock, A. D.; Dertinger, S. K.; Whitesides, G. M. *J Am Chem Soc* **2003**, *125*, 5294-5295.

(5) Jiang, X.; Xu, Q.; Dertinger, S. K.; Stroock, A. D.; Fu, T. M.; Whitesides, G. M. *Anal Chem* **2005**, *77*, 2338-2347.

(6) Mao, H.; Holden, M. A.; You, M.; Cremer, P. S. *Anal Chem* **2002**, *74*, 5071-5075.

(7) Pihl, J.; Sinclair, J.; Sahlin, E.; Karlsson, M.; Petterson, F.; Olofsson, J.; Orwar, O. *Anal. Chem.* **2005**, *77*, 3897-3903.

(8) Balss, K. M.; Ross, D.; Begley, H. C.; Olsen, K. G.; Tarlov, M. J. *J Am Chem Soc* **2004**, *126*, 13474-13479.

(9) Xie, J.; Miao, Y.; Shih, J.; He, Q.; Liu, J.; Tai, Y. C.; Lee, T. D. *Anal Chem* **2004**, *76*, 3756-3763.

(10) Mao, H.; Cremer, P. S.; Manson, M. D. *Proc Natl Acad Sci U S A* **2003**, *100*, 5449-5454.

(11) Unger, M. A.; Chou, H. P.; Thorsen, T.; Scherer, A.; Quake, S. R. *Science* **2000**, *288*, 113-116.

(12) Hansen, C. L.; Skordalakes, E.; Berger, J. M.; Quake, S. R. *Proceedings of the National Academy of Sciences of the United States of America* **2002**, *99*, 16531-16536.

[Insert Running title of <72 characters]

(13) Hansen, C. L.; Sommer, M. O.; Quake, S. R. *Proc Natl Acad Sci U S A* **2004**, *101*, 14431-14436.

(14) Taylor, S. G. *Proc. Roy. Soc. A* **1953**, *219*, 186.

(15) Aris, R. *Proc. R. Soc. London, Ser. A* **1956**, *235*, 67.

(16) Chatwin, P. C.; Sullivan, P. J. *Journal of Fluid Mechanics* **1982**, *120*, 347-358.

(17) Ajdari, A.; Bontoux, N.; Stone, H. A. *Anal Chem* **2006**, *78*, 387-392.

(18) Studer, V.; Hang, G.; Pandolfi, A.; Ortiz, M.; Anderson, W. F.; Quake, S. R. *Journal of Applied Physics* **2004**, *95*, 393-398.

(19) Chen, Y.; Müller, J. S.; Eid, J. S.; Gratton, E. *New trends in Fluorescence spectroscopy*; Springer-Verlag: Berlin, 2001.

[Insert Running title of <72 characters]

Annexe C

Exemple d'utilisation de l'équivalence électrique pour un pousse seringue

Rappels sur l'équivalence hydraulique-électrique

Comme nous l'avons vu dans le corps du texte, une équivalence électrique est possible entre un circuit microfluidique et un circuit électrique. Valable pour des écoulements monophasiques, le tableau C.1 rappelle les équivalences fluidiques-électriques ainsi que les unités adaptées à la microfluidique.

Le tableau C.2 donne les expressions de la résistance pour différentes sections de micro-canaux. Par exemple, dans le cas d'un canal rectangulaire de 300 μm de large, 10 μm de haut et de 9 cm de long, la résistance hydraulique vaut $\frac{200\times9}{1^3\times3} = 600\ \Omega l$ et la pression à appliquer vaut $P = RQ = 600 \times 10\ mBar = 6\ Bar$ si l'on veut un débit de $10\mu L/min$.

Nous rappelons ici les formules déjà données dans le corps du texte ainsi que les unités microfluidiques choisies ici.

Fluidique	Electrique	Unité microfluidique	Abréviation
Volume (m^3)	Charge (Coulomb)	1 μL	
Pression (Pa)	Potentiel (Volt)	1 mBar	
Débit (m^3/s)	Courant (Ampère)	1 $\mu L\ min^{-1}$	
Résistance ($Pa\ s\ /m^3$)	Résistance (Ohm)	1 $mBar\ min\ \mu L^{-1}$	Ωl
Capacité (m^3/Pa)	Capacité (Farade)	1 $\mu L\ mBar^{-1}$	Fl

Tab. C.1 – Equivalence entre grandeurs fluidiques et électriques. Les unités SI sont entre parenthèses.

	Tube cylindrique	Canal de section rectangulaire	Canal de section parabolique
Résistance	$\frac{0{,}68\ L_{cm}}{d^4_{100\mu m}}$	$\frac{200\ L_{cm}}{h^3_{10\mu m}\ l_{100\mu m}}$	$\frac{440\ L_{cm}}{h^3_{10\mu m}\ l_{100\mu m}}$
Expression	$\frac{128\ \mu\ L}{\pi\ d^4}$	$\frac{12\ \mu\ L}{h^3\ l}$	$\frac{105\ \mu\ L}{4\ h^3\ l}$

TAB. C.2 – Valeurs de la résistance en Ωl pour un écoulement d'eau ($\mu = 1\ mPas$) pour différents types de canaux en unité microfluidique. Les quantités en indices indiquent l'unité des longueurs : si $h = 30\ \mu m$, il faut mettre $h_{10\mu m}$=3 dans la formule. Pour le canal parabolique, h correspond à la hauteur au centre du canal.

Tube Tygon (0,51 mm×2,2 mm)	0,2 mFl/cm	Proportionnel à la longueur
Tube PE (0,51 mm×1 mm)	1 μFl /cm	Proportionnel à la longueur
Bulle d'air	1 mFl/μL	Proportionnel au volume

TAB. C.3 – Exemples de valeurs de capacité pour différents éléments. Par analogie électrique, les unités sont en Farad.

Exemple d'application de l'équivalence électrique : cas d'un pousse seringue

Si on choisit d'imposer le débit avec un pousse seringue, on peut estimer le temps de mise à l'équilibre. En utilisant un tube en tygon de 30 cm de long pour connecter la seringue au microsystème, on a une capacité de 6 mF. La résistance hydraulique est égale à 600 Ωl (la résistance du tube en tygon est négligeable). Le temps de mise à l'équilibre vaut $600 \times 0,006 = 3,7$ min. Si maintenant une bulle d'air est présente dans la seringue (typiquement 50 μL), la capacité monte à 56 mFl et le temps caractéristique de mise à l'équilibre vaut plus de 30 min. Le débit sera stable au bout de 1h30 environ !

Plus précisément, on peut faire le schéma équivalent de l'ensemble pousse-seringue microsystème. En négligeant la résistance du tube R_T, on trouve bien un temps caractéristique égale à $R_\mu C_T$. Par contre si on applique une pression aux bornes du système, la situation est complètement différente : le temps de réponse est alors égale à $R_T C_T$, qui est très court (0,01 s) : le fluide va se mettre en mouvement quasiment instantanément.

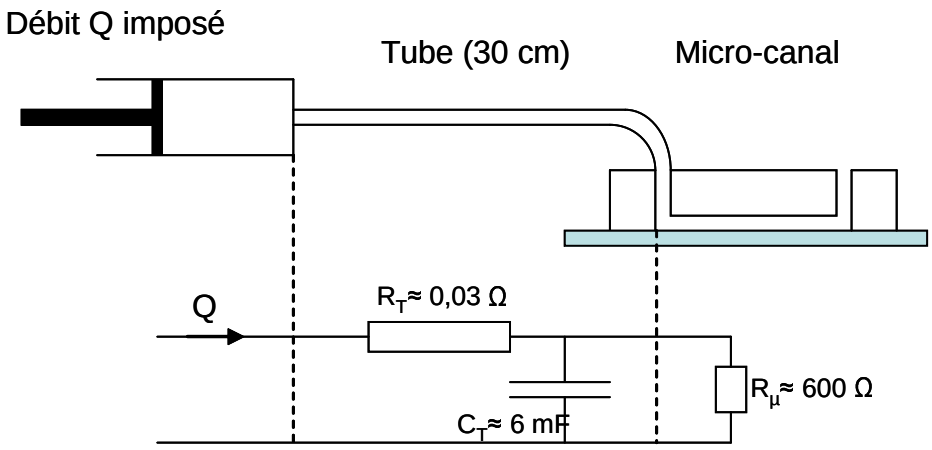

FIG. C.1 – Schéma équivalent électrique équivalent pour un ensemble pousse-seringue microcanal

Annexe D

Mélangeur-doseur utilisant la dispersion de Taylor-Aris

Principe de mélange

Le principe du mélangeur décrit ici est basé sur la dispersion de Taylor-Aris. Grâce à l'utilisation de microvannes, on peut réaliser le long d'un microcanal une succession de volumes contenant les deux liquides à mélanger. Grâce à la dispersion, les deux liquides vont s'interpénétrer, favorisant le mélange. De plus en faisant varier les rapports relatifs des volumes, le rapport de mélange entre les deux liquides est contrôlable. La figure D.1 illustre la méthode.

Mise en oeuvre et caractérisation du mélange

Le dispositif microfluidique de la plate-forme puce à ADN a été utilisé (4.2). De l'eau désionisée et une solution de fluorescéine (1 mM fluorescéine acide, 10 mM de NaOH) sont déposées dans les réservoirs. Les microvannes sélectionnent le liquide à introduire dans le canal de mélange à un débit contrôlé par la micro-pompe n°1. L'intensité de fluorescence est mesurée le long du canal après l'intersection en faisant abstraction des coudes.

Les paramètres de commande sont au nombre de trois : la vitesse du liquide dans le canal v_0, la fréquence des volumes des différents liquides f_m et le rapport de mélange R. Le mélange est caractérisé par l'amplitude résiduelle des oscillations dues à la formation

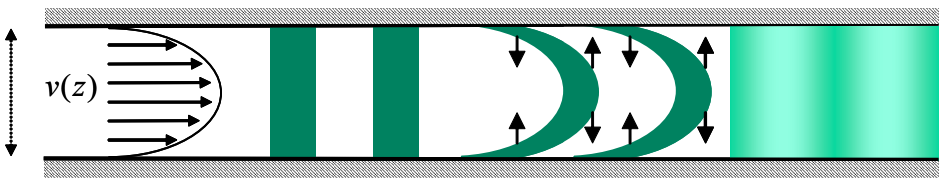

Fig. D.1 – Principe du mélangeur-doseur : une succession de volumes des deux liquides à mélanger est introduite dans le microcanal. Les différents régimes de dispersion de Taylor-Aris mélangent les liquides.

des volumes de liquide différents σ_T. On prend le même repère que dans 3.1.1, avec l'axe y orienté le long du canal, x perpendiculaire à l'écoulement et z dans la hauteur. On exprime σ_T par l'écart type du signal de fluorescence I au cours du temps.

$$\sigma_T = \frac{\sqrt{\left\langle \left(\langle I \rangle_x - \langle I \rangle_{x,t} \right)^2 \right\rangle_t}}{\langle I \rangle_{x,t}} \tag{D.1}$$

Avec $\langle I \rangle_x$ la valeur moyenne dans la largeur, $\langle I \rangle_{x,t}$ la valeur moyenne dans la largeur et dans le temps. σ_T est une fonction de y : le tracé de σ_T en fonction de y est considéré dans la suite comme caractérisant le mélange le long du canal.

Résultats expérimentaux

La figure D.2 montre une image de fluorescence du dispositif où l'on distingue le canal de mélange et les différents volumes qui se déforment sous l'action de la dispersion de vitesses. La figure D.3 montre les profils de concentration le long du canal à trois instants différents et la quantité σ_T tracé en semilog en fonction de la distance. Dans ce cas la vitesse du fluide est $v_0 = 1,9$ mm/s et la fréquence de mélange est $f_m = 0{,}5$ Hz.

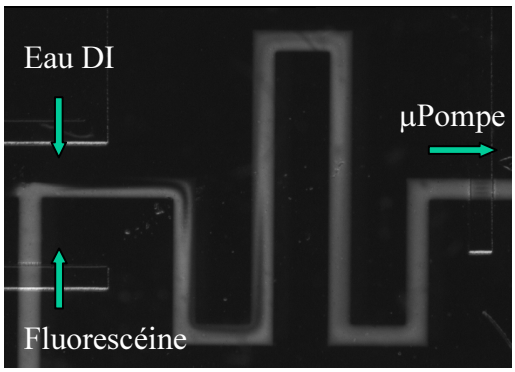

FIG. D.2 – Image du dispositif.

Le profil de σ_T a été mesuré pour différentes valeurs de vitesses v_0 (0,8 à 5,3 mm/s) et de fréquences de mélange f_m (0,5 à 2 Hz) (figure D.4) pour R=50 %. Il est apparu que l'ensemble des profils décroissait d'abord de manière exponentielle pour ensuite se stabiliser à une valeur de l'ordre de 10^{-2}. Le tracé des σ_T en fonction du temps de mélange $t = y/v_0$ montre que toutes les courbes se superposent pour une même valeur de f_m. La pente ne dépend alors que de f_m.

L'atténuation des oscillations est d'autant plus rapide que la fréquence de mélange est grande. Ceci est tout à fait comforme à l'intuition : l'interpénétration des volumes est d'autant plus rapide qu'ils occupent une petite portion du canal. Or chaque volume de liquide occupe une distance dans le canal d'envirion d=$v_0/(2f_m)$. En supposant un dispositif qui pourrait générer une succession très rapprochée de liquides différents, le mélange serait très rapide. En ce qui concerne notre dispositif, la fréquence maximum

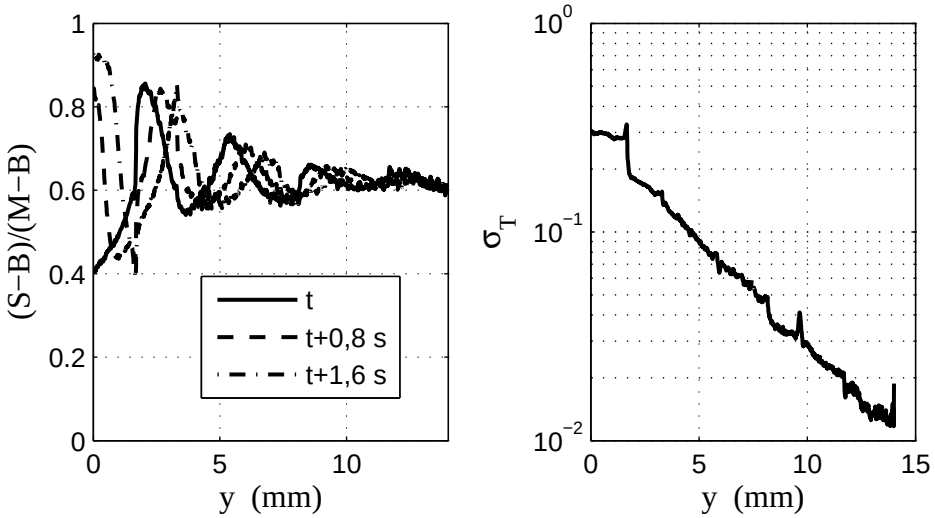

FIG. D.3 – (a) Profils de concentration le long du canal à trois instants différents. (b) σ_T en fonction de la distance de mélange tracé en semilog. La vitesse du fluide est de $v_0 = 1,7$ mm/s et la fréquence de mélange est $f_m = 0{,}5$ Hz.

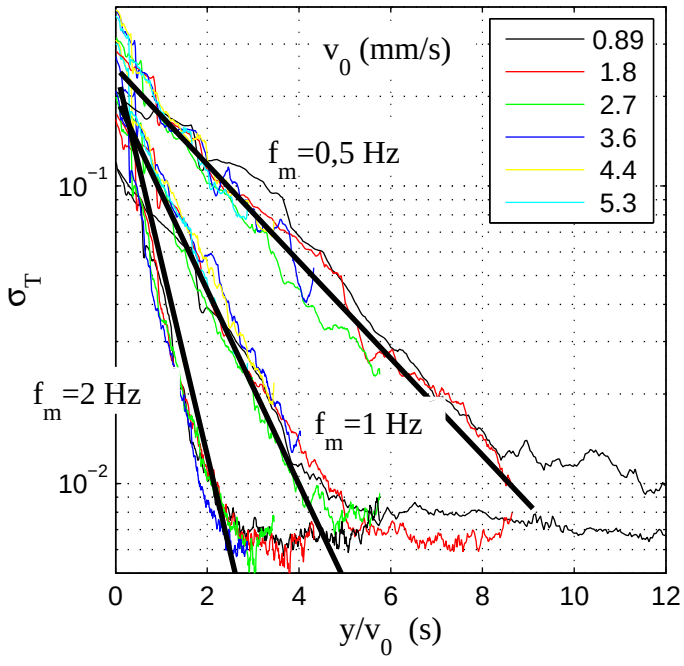

FIG. D.4 – σ_T en fonction du temps de mélange pour différentes vitesses d'écoulement v_0 et de fréquence de mélange f_m. Le rapport de mélange est de 50 %.

$f_m(Hz)$	0,5	1	2
$v_0/\lambda(s^{-1})$	$0,35 \pm 0.04$	$0,71 \pm 0.07$	$1,55 \pm 0.1$

TAB. D.1 – Valeurs des pentes réduites $v_0/\lambda(s^{-1})$, déduites des mesures précédentes, en fonction de la fréquence de mélange.

utilisable est d'environ 2 Hz. Au dessus, les volumes n'ont pas le temps de se former dans le canal à cause du volume à l'intersection des canaux.

Plus qualitativement, on peut estimer la pente en approchant les courbes par la fonction $Ae^{-y/\lambda}$. Le tableau D.1 donne les valeurs de v_0/λ pour les différentes fréquences de mélange. On observe une quasi dépendance linéaire de v_0/λ en fonction de f_m pour ces trois points de mesures.

Comparaison avec le modèles de dispersion

Nous avons détaillé les différents régimes de dispersion de Taylor-Aris dans la partie 3 ainsi que leur limite de validité. Pour les dimensions de notre dispositif (w=300 μm, h_0 =32 μm et $D_t h = 3\ 10^{-10}\ m^2/s$), le régime à temps court est établi entre 0,15 s et 10,5 s (tableau 3.1). Dans le cas présent, le régime à temps court est pertinent (t<10 s).

Ce régime a été modélisé précédement (3.2.2) pour la dispersion d'une interface entre deux liquides contenant une espèce diffusante. Nous avons affaire ici à une succession d'interfaces séparées d'une distance d=$v_0/(2f_m)$, chacune étant modélisable par la relation 3.7 et 3.8.

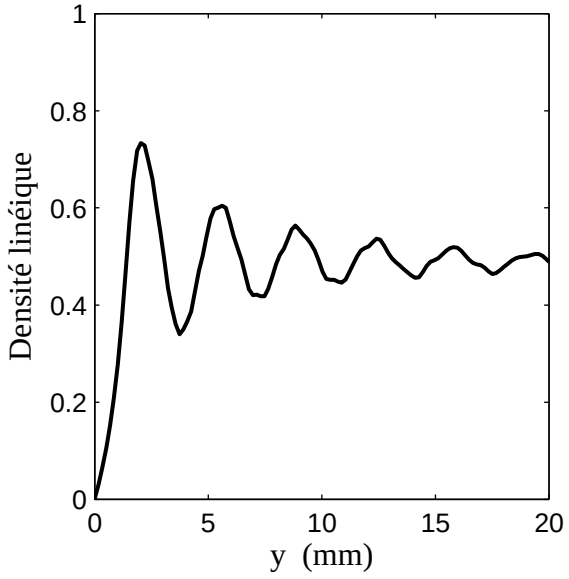

FIG. D.5 – Simulation des données expérimentales de la figure D.3 grâce au modèle présenté au chapitre 2.

La figure D.5 montre les oscillations résiduelles de la densité linéique de fluorescence dans les mêmes conditions expérimentales que celles de la figure D.3. On observe un accord

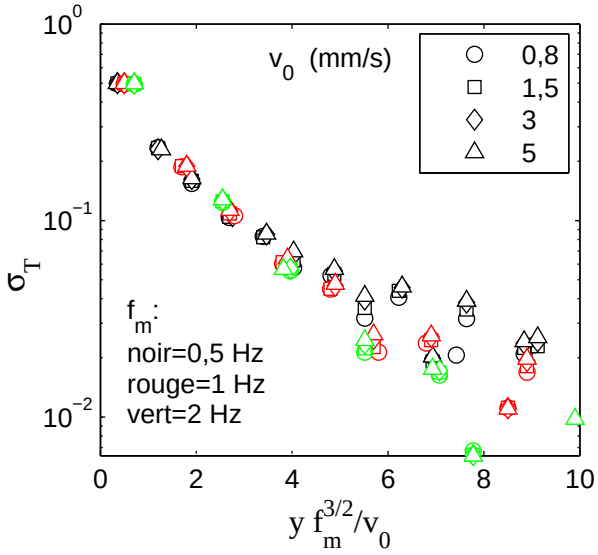

FIG. D.6 – Simulation de σ_T avec le modèle développé au chapitre 2 pour le régime à temps court de Taylor-Aris.

quasi quantitatif étant donné que l'on a complètement ignoré les coins des canaux.

σ_T est estimé à partir de courbe comme celle de la figure D.5 : à chaque période d'oscillation, l'amplitude des oscillations est mesurée par rapport à la moyenne égale à 0,5. Cette grandeur est égale à σ_T à un facteur multiplicatif près.

Sur la figure D.6, les σ_T sont tracés pour différentes conditions expérimentales (f_m=0,5 à 2 Hz et v_0=0,8 à 5 mm/s) correspondant à nos mesures. Si les données sont tracées en fonction de $yf_m^{3/2}/v_0$, les courbes se superposent : la distance caractéristique d'atténuation des oscillations est proportionnelle à $v_0/f_m^{3/2}$. Pour des raisons de dimension, la racine d'un temps doit être multipliée à cette quantité pour être homogène à une distance. Un temps caractéristique naturel est le temps de diffusion dans la hauteur h_0^2/D_{th}. Ceci suggère que la distance caractéristique est proportionnelle à $v_0/f_m \times \sqrt{D_{th}/(h_0^2 f_m)}$ [1].

Malgré les approximations de la détermination de σ_T dans la simulation et l'absence de prise en compte des coins, le modèle du régime à temps court rend très bien compte des mesures expérimentales. A la fois dans les simulations et l'expérience, la distance d'atténuation des oscillations est proportionnelle à la vitesse de l'écoulement. Pour la fréquence de mélange, la dépendance trouvée dans les simulations est compatible avec les mesures. Si les données expérimentales de la figure D.4 sont tracées en fonction de yf_m^n/v_0 , les courbes se superposent pour n=1,3, valeur proche de 1,5 trouvée théoriquement.

1. Nous avons vérifié cette relation sur un ordre de grandeur pour chacune des variables D_{th}, h_0, f_m et v_0.

Conclusion

La dispersion de Taylor-Aris a été mise en oeuvre ici pour réaliser des mélanges entre deux liquides. Grâce aux micro-actuateurs, des volumes successifs de deux liquides sont envoyés dans un microcanal : la dispersion de Taylor-Aris mélange les deux liquides. Avec le critère de mélange σ_T qui mesure les oscillations résiduelles de concentration, une distance de mélange de l'ordre de $0{,}75 v_0/f_m$ a été trouvée expérimentalement.

Des simulations du régime à temps court de la dispersion de Taylor-Aris (3.2.2) ont été réalisées montrant un bonne accord avec les mesures. La distance de mélange est apparue proportionnelle à $v_0/f_m^{3/2}$. Etant données les approximations de la simulation et la précision des mesures, nos simulations sont compatibles avec les mesures.

Annexe E

Fabrication du microsystème puce à ADN

Le microsystème en PDMS est fabriqué à l'aide de la technologie MSL décrite dans le premier chapitre. Pour finaliser la réalisation du microsystème intégrant la puce à ADN, la suite du protocole se déroule comme suit :

Insertion du thermocouple

Le thermocouple de 80 μm de type K est glissé dans l'un des canaux d'actuation de la μpompe 2. La condamnation d'une des trois vannes permet toujours le pompage selon un cycle adapté. Après avoir maintenu le microsystème sous un vide faible durant 1 heure, du PDMS mélangé avec du réticulant est versé au niveau de l'insertion. Le PDMS est alors aspiré à l'intérieur du canal et le remplit totalement, évitant toutes bulles d'air. Le système est alors réticulé durant 2 heures à 75°C.

Collage du microsystème sur la puce

Pour les supports fabriqués par la société Genescore, la procédure est la suivante :

1. Rinçage des surfaces de PDMS et de la lame de verre spotée à l'éthanol absolu puis séchage à l'air.
2. Alignement de la chambre d'hybridation, à l'oeil ou sous binoculaire sur la zone spotée préalablement repérée.
3. Mise au four durant 2 heures à 75°C.

Dans le cas d'autres supports (Schott ou CodeLink), le collage est plus délicat et nécessite l'activation des surfaces par plasma O_2 ou équivalent. Pendant cette étape, les spots doivent être protégés :

1. Rinçage des surfaces de PDMS et de la lame de verre spotée à l'éthanol absolu puis séchage à l'air.

2. Masquage de la zone spotée par une couche de PDMS de taille comparable.
3. Passage au plasma des deux parties à coller.
4. Après avoir enlevé le masquage, alignement de la chambre d'hybridation, à l'oeil sur la zone spotée préalablement repérée.

Préparation du microsystème

Suivant une procédure brevetée [19], le système comprenant la lame de verre spotée et le thermocouple sont placés sous un vide partiel durant au moins 5 heures.

Procédure de remplissage

Dès la sortie du vide, les extrémités des canaux (réservoirs et sortie) doivent être remplis avec du tampon. Le système se remplit alors tout seul. Les tubes de pression activant les microactuateurs sont connectés.

Réchauffeur

Sur une lame de verre de $50 \times 75 \times 1$ mm, les pistes d'or de 100 nm d'épaisseurs sont réalisées par des techniques classiques de microfabrication : évaporation de 3 nm de chrome et de 100 nm d'or puis attaque chimique localisée après masquage par une résine positive des motifs.

Pour améliorer le contact thermique entre l'or des pistes et la lame de verre supérieure, une fine couche de contacteur thermique (300 μm) recouvre les pistes. L'ensemble est délicatement serré par des mâchoires disposées sur la platine (voir figure 4.6 A).

Précautions indispensables

Lors de changement de liquide dans les réservoirs, il est nécessaire de rincer celui-ci pour éviter toute contamination. Généralement, un rinçage à la formamide pure suivi de trois rinçages à l'eau désionisée sont effectués.

Annexe F

Automate de régulation de température

La fonction de régulation de la température se fait via un programme LabView. Une carte National Instrument permet l'acquisition de la température par mesure directe de la tension aux bornes du thermocouple. Ce signal est traité grâce au programme. La commande de chauffage résultante est donnée à un circuit de puissance extérieure via la même carte.

Le transfert de puissance se fait grâce à un relais statique (transistor darlington) commandé par un signal carré de fréquence 30 Hz. C'est le rapport cyclique e du signal qui contrôle la puissance dissipée à la résistance : e étant le rapport de temps où le relais statique est fermé sur le temps total, une fraction e de la puissance maximale délivrable (U^2/R) est transmise à la résistance.

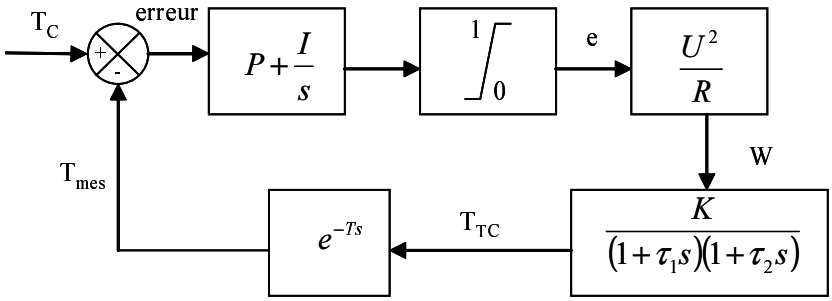

FIG. F.1 – Fonction de transfert de la modélisation du comportement thermique de la plateforme microfluidique.

Pour stabiliser la température de la plate-forme microfluidique, nous avons modélisé son comportement thermique sous forme d'une fonction de transfert. Le schéma F.1 montre les différents blocs de traitements. s est la variable de Laplace. La différence entre la température mesurée T_{mes} et la température consigne T_C est injectée dans un intégrateur-proportionnel dont les paramètres (P et I) sont critiques pour le temps de réponse du système et sa stabilité. Après écrêtage entre 0 et 1 du signal de commande, le rapport cyclique e est envoyé grâce à la carte sur le relais statique qui transmet une

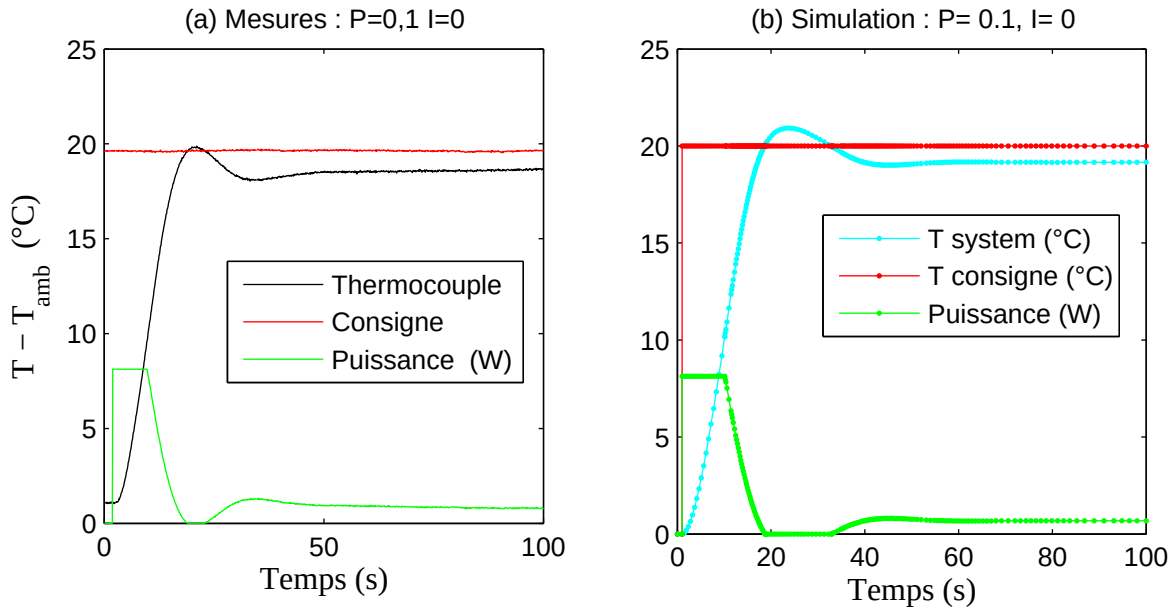

FIG. F.2 – (a) mesure du comportement du système pour un échelon de température. (b) simulation associée avec le modèle.

puissance eU^2/R à la plate-forme. Une fonction de transfert modélise le comportement de la plate-forme. Un retard T est inséré pour prendre en compte le temps de traitement de l'ordinateur.

Les paramètres directement accessibles ont pour valeur R=12,3 Ω, U=10 V et T=0,11 s. Grâce à une modélisation réalisée sous Matlab Simulink, nous avons pu, par comparaison avec des expériences, estimer les paramètres restants : K=28°C/W, τ_1=120 s et τ_1=4 s (figure F.2).

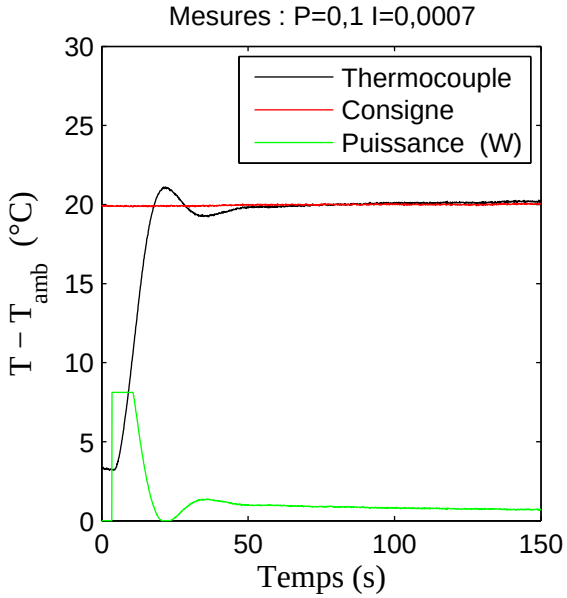

FIG. F.3 – Mesures de la régulation thermique pour les paramètres P et I optimaux.

Le modèle étant déterminé, les paramètres P et I ont été choisis pour diminuer le temps de réponse, tout en ayant une erreur nulle et une surchauffe minimale. Nous avons

trouvé que P=0,1 et I=0,0007 fournissaient les meilleurs résultats. La figure F.3 montre des mesures de température pour ce réglage. L'erreur de température par rapport à la consigne est nulle au bout de 60 s avec une surchauffe de 1,6°C. La stabilité en température est meilleure que $\pm 0,05$°C.

Annexe G

Photoblanchiment et réaction d'hybridation : critère de précision

Les fluorophores sont susceptibles de se détruire sous l'action de la lumière avec un temps caractéristique proportionnel à l'intensité lumineuse, τ_b. Soit N^* le nombre de fluorophores fonctionnels hybridés sur la puce, N le nombre de fluorophores non-fonctionnels hybridés sur la puce et N_T le nombre total de site d'hybridation. En prenant en compte la cinétique d'hybridation, supposée de Langmuir et le photoblanchiment, on obtient les équations bilans suivantes :

$$\dot{N^*} = k_a C(N_T - N^* - N) - k_d N^* - \frac{1}{\tau_b} S(t) N^* \quad \text{(G.1)}$$

$$\dot{N} = \frac{1}{\tau_b} S(t) N^* - k_d N \quad \text{(G.2)}$$

Avec $S(t) = 1$ si l'échantillon est illuminé et 0 sinon. On suppose que les ouvertures et fermetures du shutter sont rapides devant la cinétique du phénomène : on considère seulement la valeur moyen de S en fonction du temps dans la suite. Le temps de photoblanchiment est alors redéfini par $\tau_b' = \tau_b / \langle S \rangle$.

Quatre termes adimensionnées N^*/N_T, $t(k_a C + k_d)$, $k_d \tau_b'$ et $K_a C$ sont nécessaires pour décrire le comportement de l'équation G.2. Après résolution analytique, la figure G.1 montre les allures typiques des courbes pour différentes valeurs de $k_d \tau_b'$ pour $K_a C = 10$. L'erreur due au photoblanchiment est mesurée par l'écart relatif à la courbe sans photoblanchiment au temps $3/(k_a C + k_d)$. La figure G.1 montre l'erreur relative en logarithme décimal pour différentes valeurs de $k_d \tau_b'$ et de $K_a C$. On en déduit un critère simple, confirmé analytiquement, pour lequel l'erreur est inférieure 5 % :

$$k_a C \tau_b' > 100 \quad \text{(G.3)}$$

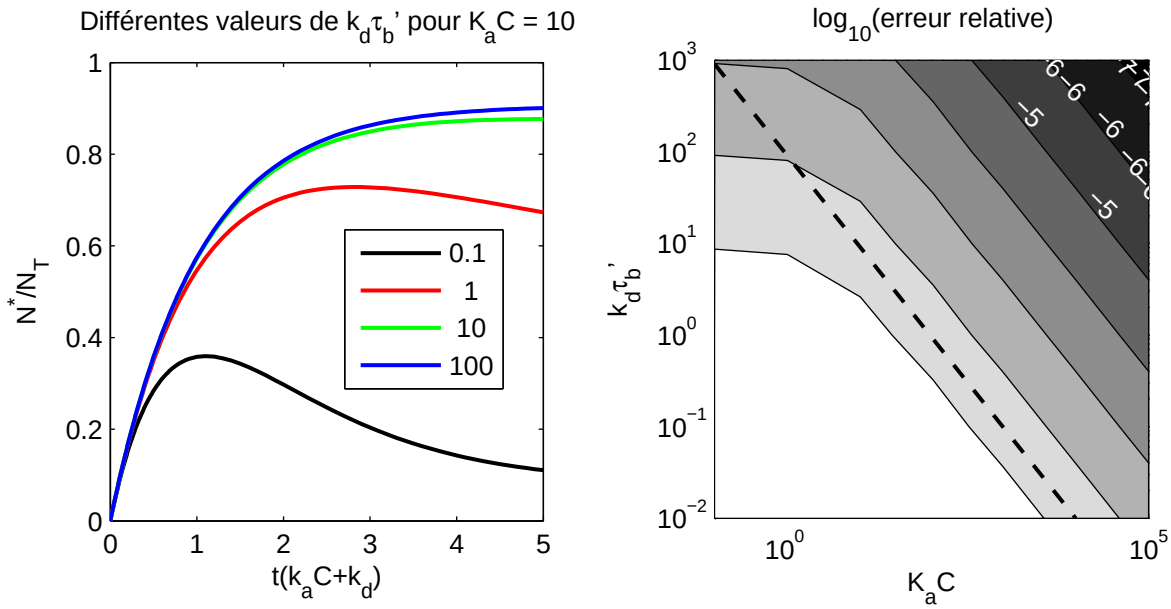

FIG. G.1 – A guache effet du photoblanchiment sur les mesures d'hybridation. A droite, erreur relative due au photoblanchiment pour différents paramètres. La courbe en pointillée est le critère G.3.

Annexe H

Description des puces à ADN utilisées

Sondes ADN

Grâce à la société Genescore, nous avons pu bénéficier de puces à ADN réalisées par spotting sur des supports commerciaux propriétaires. Les sondes greffées sur les supports sont des oligonucléotides synthétiques achetés auprès de la société IBA, qui sont fonctionnalisés avec un groupement NH_2 permettant le greffage covalent sur la surface. Le tableau H.1 donne la séquence des sondes utilisées. Ces séquences correspondent à des fractions de gènes de récepteur du glutamate chez la sourie *Mus Musculus*. Ces séquences ont été choisies par Genescore selon les critères suivants :

- Température de fusion proche,
- Faible structure secondaire,
- Spécificité uniquement avec le gène considéré.

	Séquence ($5' \rightarrow 3'$)
Sonde 1	NH2- GTGCCTCACGGTGGTTGCCATCACTGTCTTCATGTTCGAGTATTTCAGCC-3'
Sonde 1-R	NH2- GTGGTTGCCATCACTGTCTTCATGTTCGAGTATTTCAGCC-3'
Sonde 1-M	NH2- GTGCCTCACGGTGGTTGCCATCAC**G**GTCTTCATGTTCGAGTATTTCAGCC-3'
Sonde 2	NH2- TTTTGAGATCTGGCTTCATTTCGACGCTGACGGAAGTGGTTACCTGGAAG-3'
Sonde 2-R	NH2- TGGCTTCATTTCGACGCTGACGGAAGTGGTTACCTGGAAG-3'
Sonde 2-M	NH2- TTTTGAGATCTGGCTTCATTTCGAC**T**CTGACGGAAGTGGTTACCTGGAAG-3'
Sonde 3	NH2- AACGCCCATCTTAAAATCGACGCCTGTCTCTCCCCCATTGCTCTTACCAG-3'
Sonde 3-R	NH2- TTAAAATCGACGCCTGTCTCTCCCCCATTGCTCTTACCAG-3'
Sonde 3-M	NH2- AACGCCCATCTTAAAATCGACGCC**A**GTCTCTCCCCCATTGCTCTTACCAG-3'

Tab. H.1 – Séquence d'ADN sondes utilisée ici. Les préfixes -R et -M désignent respectivement les oligos réduits de 10 bases, et modifiés d'une base (en gras).

Plan de puce

Le plan de puce est l'agencement des différents spots sur la surface de la lame de verre. Il est constitué d'un motif de base que l'on répète plusieurs fois sur la puce. Pour notre système microfluidique, le plan de puce devait répondre aux contraintes suivantes :

- Les lames de verre ont le format standard $25 \pm 1\ mm \times 75 \pm 1\ mm$.
- Le motif de base doit être inférieure à $1,35\ mm \times 1,35\ mm$ (zone d'observation de la caméra à l'objectif $\times 10$).
- Le motif de base est répété au moins 9 fois en matrice 3 par 3,
- Le centre des motifs est positionné à $11 \pm 1\ mm$ et à $37,5 \pm 1\ mm$ du coin de la lame.

Deux plans de puce ont été réalisés, le motif "Qualité" et "SNP". Ils sont décrits aux tableaux H.3 et H.2. La figure H.1 montre les images de fluorescence des motifs après hybridation.

	$\emptyset$	$\emptyset$	$\emptyset$	NH_2	NH_2	NH_2
$5\mu M$	Sonde 1	Sonde 2	Sonde 3	Sonde 1	Sonde 2	Sonde 3
$10\mu M$	Sonde 1	Sonde 2	Sonde 3	Sonde 1	Sonde 2	Sonde 3
$20\mu M$	Sonde 1	Sonde 2	Sonde 3	Sonde 1	Sonde 2	Sonde 3
$40\mu M$	Sonde 1	Sonde 2	Sonde 3	Sonde 1	Sonde 2	Sonde 3

Tab. H.2 – Motif de base du plan de puce "Qualité", comprenant 6×4 spots. Chaque ligne correspond à une concentration de spotting. Les ADN sondes des trois premières colonnes ne sont pas fonctionnalisés NH_2, contrairement aux trois dernières.

Cy3				Cy3
	Sonde 3	Sonde 3-M	Sonde 3-R	
	Sonde 2	Sonde 2-M	Sonde 2-R	
	Sonde 1	Sonde 1-M	Sonde 1-R	
Cy3				Cy3

Tab. H.3 – Motif de base du plan de puce "SNP". Chaque case du tableau correspond à un spot. l'interspot est de $200\mu m$. La concentration de spotting est de 15 μM. Cy3 correspond à des sondes 2 marquées Cy3.

Protocole de greffage des puces Genescore

Le protocole de greffage et de spotting de la société Genescore se compose de 4 étapes, décrites succinctement :

- La surface de verre est silanisée.
- Sur ces silanes possédant une fonction -SH, un PEG (PolyEthylèneGlycol) bi-fonctionnel est greffé. Cette molécule va jouer le rôle d'espaceur entre le silane et l'ADN sonde.
- Des oligos sondes modifiés -NH_2 sont spottés sur la lame de verre. Ils réagissent avec l'extrémité libre fonctionalisée -NHS du PEG, assurant ainsi un greffage covalent.
- Les sites -NHS du PEG qui n'ont pas réagi sont passivés (capping).

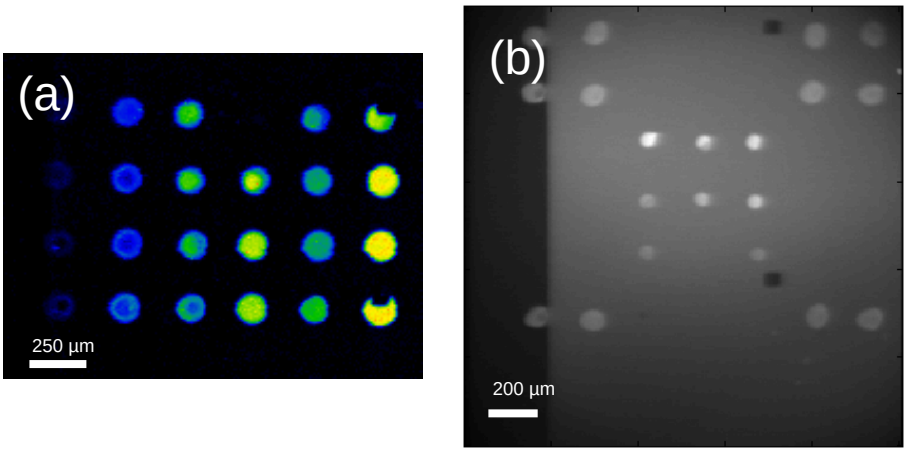

FIG. H.1 – Images réalisées après hybridation pour les deux plans de puce utilisés : (a) "Qualité" et (b) "SNP". L'abscence du spot sondes 1-M sur la photo (b) est due à l'abscence de greffage des sondes.

Les lames sont alors prêtes à être utilisées.

Silanisation

Des lames de verre au format 25 $mm \times 75$ mm du commerce (Gold Seal, VWR) sont nettoyées avec un mélange Piranha (acide sulfurique/eau oxygénée 350mL/150mL) pendant 15 min. Après plusieurs rinçages à l'eau MilliQ, un dernier rinçage au méthanol est effectué pendant 5 min.

Pour 10 lames, 5,32 mL de silane 3-Mercaptopropyl-triméthoxysilane (Aldrich n°17,561-7) est ajouté au dernier moment dans une solution contenant 250 mL de méthanol, 2,13 mL d'acide acétique et 10,6 mL d'eau MilliQ. Les lames sont alors plongées dans la solution pendant 4 heures à température ambiante.

Après plusieurs rinçage au méthanol, les lames sont séchées et mises au four à 100°C pendant une nuit. Les lames sont alors stockées dans une boîte propre.

Greffage du PEG (espaceur)

Dans 200 μL de tampon PBS 1X, 0,75 mg de PEG bi-fonctionnel (NHS-PEG-VS) de masse moléculaire 3400 g/mol (Shearwater Polymers) est rajouté. L'ensemble est déposé sur la lame de verre silanisée à température ambiante pendant 45 min. Un film de parafilm est placé sur la lame pour diminuer l'évaporation.

Après deux rinçages à l'eau MilliQ, les lames sont séchées à la centrifugeuse (5 min à 800 tr/min). Les groupements -NHS étant très sensibles à l'humidité, le spotting doit se faire le plus tôt possible après cette étape.

Spotting des oligonucléotides

Le spotting est une technique de dépôt local d'oligonucléotides à l'aide d'une pointe creuse venant au contact avec la lame de verre. La taille des spots est typiquement de 100 μm de diamètre. Nous avons utilisé le spotteur Biorobotics Microgrid II avec les réglages habituels utilisés par Genescore. Le tampon de spotting est 150 mM de tampon phosphate à pH=8,3. La concentration typique d'oligonucléotides sondes est de 10 μM.

Passivation des sites de greffages encore actifs.

Les groupements -NHS des PEG qui n'ont pas réagis sont passivés par une petite amine (éthanolamine, E-9508, Sigma Aldrich). Pour un volume final de 1 L complété par de l'eau MilliQ, la solution de passivation contient 200 mL de Tris-HCl 0,5 M pH=9 et 3 mL d'éthanolamine. Les lames sont mises en contact avec cette solution pendant 30 min à 50°C puis rincées deux fois à l'eau MilliQ.

Un rinçage avec une solution contenant 4X SSC et $0,1\%$ SDS préalablement chauffée à 50°C est effectué à température ambiante pendant 30 min. Après deux rinçages à l'eau MilliQ, les lames sont séchées à la centrifugeuse. Elles sont prêtes à l'emploi et doivent être stockées à l'abrit de la lumière.

Annexe I

Résultats des dosages d'allèles sur des échantillons sanguins

Grâce au travail de Paul Kauffmann et de Marie-Claude Potier, le protocole biologique décrit au paragraphe 6.4 a pu être réalisé et optimisé. A la fin de ce protocole, une quantité significative d'ADN simple brin marqués Cy3 d'environ 200 bases de long est suspendue dans la solution d'hybridation décrite précédemment.

Suivant le protocole décrit au paragraphe 6.2.2, les expériences ont d'abord été réalisées à 35°C. Le signal d'hybridation était alors trop faible et la température d'hybridation a été baissée à 30°C, fournissant ainsi un signal suffisant.

La région contenant le SNP rs722557 (tableau 6.2) a été spécifiquement amplifiée pour 4 patients différents de génotype TT, CTT, CCT et CCC. Le tableau I.1 montre pour chaque patient le résultat du dosage réalisé dans le dispositif microfluidique (exprimé par $C/(C+T)\%$) en fonction du génotype déterminé par RFLP et séquençage. On remarque que la précision de la méthode est maintenue sur des échantillons biologiques issus directement de patients trisomiques.

Génotype	$C/(C+T)\%$
TT	0%
CTT	$37 \pm 7\%$
CCT	$65 \pm 7\%$
CCC	$98 \pm 2\%$

Tab. I.1 – Comparaison entre le génotype déterminé par RFLP et séquençage et le pourcentage $C/(C+T)\%$ dterminé par la méthode présentée au paragraphe 6.4. Cette mesure permet une détermination sans ambiguïté du génotype.

Cette méthode qui montre ici sa robustesse, permet de déterminer sans ambiguïté le génotype du patient. De plus les échantillons des quatre patients ont été mesurés sur le même dispositif, après un rinçage approprié, sans montré de contamination croisée.

En conclusion cette méthode a été validée ici sur des échantillons biologiques et permet le dosage d'allèle à une précision de $\pm 10\%$ et ceci en 30 min sur un dispositif réutilisable au moins 20 fois. Il reste à valider la possibilité de doser plusieurs allèles simultanément, performance qui semble tout à fait accessible à la vue de l'étude détaillée des résultats expérimentaux. Potentiellement, ce dispositif pourrait doser simultanément 250 allèles. Cette méthode convient tout à fait à la problèmatique de l'IGH de Montpellier et est comparable aux différentes méthodes existantes [125, 137, 138].

Bibliographie

[1] P. Joseph and P. Tabeling. Direct measurement of the apparent slip length. *Physical Review E*, 71(3) :–, 2005.

[2] A. Manz, N. Graber, and H. M. Widmer. Miniaturized total chemical-analysis systems - a novel concept for chemical sensing. *Sensors and Actuators B-Chemical*, 1(1-6) :244–248, 1990.

[3] R. H. Liu, J. Yang, R. Lenigk, J. Bonanno, and P. Grodzinski. Self-contained, fully integrated biochip for sample preparation, polymerase chain reaction amplification, and dna microarray detection. *Anal Chem*, 76(7) :1824–31, 2004.

[4] M. A. Unger, H. P. Chou, T. Thorsen, A. Scherer, and S. R. Quake. Monolithic microfabricated valves and pumps by multilayer soft lithography. *Science*, 288(5463) :113–116, 2000.

[5] T. Deng, H. Wu, S. T. Brittain, and G. M. Whitesides. Prototyping of masks, masters, and stamps/molds for soft lithography using an office printer and photographic reduction. *Anal Chem*, 72(14) :3176–80, 2000.

[6] V. Studer, A. Pepin, Y. Chen, and A. Ajdari. An integrated ac electrokinetic pump in a microfluidic loop for fast and tunable flow control. *Analyst*, 129(10) :944–949, 2004.

[7] B. Lonetti, J. Goulpeau, A. Ajdari, and P. Tabeling. Producing controlled concentration gradients along microchannels. In K. F. Jensen, J. Han, D. J. Harrison, and J. Voldman, editors, *microTAS2005*, volume 2, page 1121, Boston, MA, USA, 2005.

[8] J. Goulpeau, D. Le Clerre, F. Richard, L. Talini, D. Trouchet, and P. Tabeling. High-throughput real time measurements of dna hybridization in a double layer polydimethylsiloxane microsystem. In K. F. Jensen, J. Han, D. J. Harrison, and J. Voldman, editors, *MicroTAS2005*, volume 1, page 319, Boston, MA, USA, 2005.

[9] S. A. Booth, M. A. Drebot, I. E. Martin, and L. K. Ng. Design of oligonucleotide arrays to detect point mutations : molecular typing of antibiotic resistant strains of neisseria gonorrhoeae and hantavirus infected deer mice. *Mol Cell Probes*, 17(2-3) :77–84, 2003.

[10] B. W. Kirk, M. Feinsod, R. Favis, R. M. Kliman, and F. Barany. Single nucleotide polymorphism seeking long term association with complex disease. *Nucleic Acids Res*, 30(15) :3295–311, 2002.

[11] A. Halperin, A. Buhot, and E. B. Zhulina. Hybridization isotherms of dna microarrays and the quantification of mutation studies. *Clin Chem*, 50(12) :2254–62, 2004.

[12] W. A. Little. Microminiature refrigeration - small is better. *Physica B and C*, 110(1-3) :2001–2009, 1982.

[13] M. Madou. *Fundamentals of Microfabrication*. CRC Press, 1997.

[14] J. Leng, B. Lonetti, P. Tabeling, M. Joanicot, and A. Ajdari. Microevaporators for kinetic exploration of phase diagrams. *Phys Rev Lett*, 96(8) :084503, 2006.

[15] M. Heckele and W. K. Schomburg. Review on micro molding of thermoplastic polymers. *Journal of Micromechanics and Microengineering*, 14(3) :R1–R14, 2004. TY - JOUR.

[16] Whitesides G. M. Xia, Y. Soft lithography. *Angew. Chem. Int. Ed.*, 37 :550–575, 1998.

[17] V. Studer, G. Hang, A. Pandolfi, M. Ortiz, W. F. Anderson, and S. R. Quake. Scaling properties of a low-actuation pressure microfluidic valve. *Journal of Applied Physics*, 95(1) :393–398, 2004.

[18] K. Nagai B. D. Freeman I. Pinnau T. C. Merkel, V. I. Bondar. Gas sorption, diffusion, and permeation in poly(dimethylsiloxane). *Journal of Polymer Science Part B : Polymer Physics*, 38(3) :415–434, 2000.

[19] J. Goulpeau. Remplissage d'un microsystème fluidique, January 18, 2005 2005.

[20] T. Gervais, J. El-Ali, A. Gunther, and K. F. Jensen. Flow-induced deformation of shallow microfluidic channels. *Lab Chip*, 6(4) :500–7, 2006.

[21] William H. Grover, Alison M. Skelley, Chung N. Liu, Eric T. Lagally, and Richard A. Mathies. Monolithic membrane valves and diaphragm pumps for practical large-scale integration into glass microfluidic devices. *Sensors and Actuators B : Chemical*, 89(3) :315–323, 2003.

[22] J. M. Berg, R. Anderson, M. Anaya, B. Lahlouh, M. Holtz, and T. Dallas. A two-stage discrete peristaltic micropump. *Sensors and Actuators A : Physical*, 104(1) :6–10, 2003. TY - JOUR.

[23] S. G. Taylor. dispersion of soluble matter in solvent flowing slowly through a tube. *Proc. Roy. Soc. A*, 219 :186, 1953.

[24] R. Aris. On the dispersion of a solute in a fluid flowing through a tube. *Proc. R. Soc. London, Ser. A*, 235 :67, 1956.

[25] P. C. Chatwin and P. J. Sullivan. The effect of aspect ratio on longitudinal diffusivity in rectangular channels. *Journal of Fluid Mechanics*, 120(JUL) :347–358, 1982.

[26] A. Ajdari, N. Bontoux, and H. A. Stone. Hydrodynamic dispersion in shallow microchannels : the effect of cross-sectional shape. *Anal Chem*, 78(2) :387–92, 2006.

[27] B. Zheng, C. J. Gerdts, and R. F. Ismagilov. Using nanoliter plugs in microfluidics to facilitate and understand protein crystallization. *Curr Opin Struct Biol*, 15(5) :548–55, 2005.

[28] C. L. Hansen, E. Skordalakes, J. M. Berger, and S. R. Quake. A robust and scalable microfluidic metering method that allows protein crystal growth by free interface diffusion. *Proceedings of the National Academy of Sciences of the United States of America*, 99(26) :16531–16536, 2002.

[29] N.L. Jeon, H. Baskaran, S. K. Dertinger, G. M. Whitesides, L. Van de Water, and M. Toner. Neutrophil chemotaxis in linear and complex gradients of interleukin-8 formed in a microfabricated device. *Nat Biotechnol*, 20(8) :826–30, 2002.

[30] S. Morgenthaler, S. Lee, S. Zurcher, and N.D. Spencer. A simple, reproducible approach to the preparation of surface-chemical gradients. *Langmuir*, 19(25) :10459–10462, 2003.

[31] N. L. Jeon, S. K. W. Dertinger, D. T. Chiu, I. S. Choi, A. D. Stroock, and G. M. Whitesides. Generation of solution and surface gradients using microfluidic systems. *Langmuir*, 16(22) :8311–8316, 2000.

[32] J. B. Salmon, C. Dubrocq, P. Tabeling, S. Charier, D. Alcor, L. Jullien, and F. Ferrage. An approach to extract rate constants from reaction - diffusion dynamics in a microchannel. *Analytical Chemistry*, 77(11) :3417–3424, 2005.

[33] H. Mao, M. A. Holden, M. You, and P. S. Cremer. Reusable platforms for high-throughput on-chip temperature gradient assays. *Anal Chem*, 74(19) :5071–5, 2002.

[34] H. Mao, T. Yang, and P. S. Cremer. A microfluidic device with a linear temperature gradient for parallel and combinatorial measurements. *J Am Chem Soc*, 124(16) :4432–5, 2002.

[35] V. V. Abhyankar, M. A. Lokuta, A. Huttenlocher, and D. J. Beebe. Characterization of a membrane-based gradient generator for use in cell-signaling studies. *Lab Chip*, 6(3) :389–93, 2006.

[36] J. Pihl, J. Sinclair, E. Sahlin, M. Karlsson, F. Petterson, J. Olofsson, and O. Orwar. Microfluidic gradient-generating device for pharmacological profiling. *Anal. Chem.*, 77(13) :3897–3903, 2005.

[37] D. Irimia, D. A. Geba, and M. Toner. Universal microfluidic gradient generator. *Anal Chem*, 78(10) :3472–7, 2006.

[38] Patrick O. Brown and David Botstein. Exploring the new world of the genome with dna microarrays. *Nat Genet*, 21(supplement) :33, 1999.

[39] Mark Schena, Dari Shalon, Ronald W. Davis, and Patrick O. Brown. Quantitative monitoring of gene expression patterns with a complementary dna microarray. *Science*, 270(5235) :467–470, 1995.

[40] P. T. Spellman, G. Sherlock, M. Q. Zhang, V. R. Iyer, K. Anders, M. B. Eisen, P. O. Brown, D. Botstein, and B. Futcher. Comprehensive identification of cell cycle-regulated genes of the yeast saccharomyces cerevisiae by microarray hybridization. *Mol Biol Cell*, 9(12) :3273–97, 1998.

[41] Richard P. Auburn, David P. Kreil, Lisa A. Meadows, Bettina Fischer, Santiago Sevillano Matilla, and Steven Russell. Robotic spotting of cdna and oligonucleotide microarrays. *Trends in Biotechnology*, 23(7) :374–379, 2005.

[42] R. J. Lipshutz, S. P. Fodor, T. R. Gingeras, and D. J. Lockhart. High density synthetic oligonucleotide arrays. *Nat Genet*, 21(1 Suppl) :20–4, 1999.

[43] G. H. W. Sanders and A. Manz. Chip-based microsystems for genomic and proteomic analysis. *Trac-Trends in Analytical Chemistry*, 19(6) :364–378, 2000.

[44] J. Vanderhoeven, K. Pappaert, B. Dutta, P. Vanhummelen, G. V. Baron, and G. Desmet. Exploiting the benefits of miniaturization for the enhancement of dna microarrays. *Electrophoresis*, 25(21-22) :3677–86, 2004.

[45] K. Pappaert, P. Van Hummelen, J. Vanderhoeven, G. V. Baron, and G. Desmet. Diffusion-reaction modelling of dna hybridization kinetics on biochips. *Chemical Engineering Science*, 58(21) :4921–4930, 2003.

[46] D. R. Dorris, A. Nguyen, L. Gieser, R. Lockner, A. Lublinsky, M. Patterson, E. Touma, T. J. Sendera, R. Elghanian, and A. Mazumder. Oligodeoxyribonucleotide probe accessibility on a three-dimensional dna microarray surface and the effect of hybridization time on the accuracy of expression ratios. *BMC Biotechnol*, 3 :6, 2003.

[47] A. Y. Fu, C. Spence, A. Scherer, F. H. Arnold, and S. R. Quake. A microfabricated fluorescence-activated cell sorter. *Nature Biotechnology*, 17(11) :1109–1111, 1999.

[48] M. C. Breadmore, K. A. Wolfe, I. G. Arcibal, W. K. Leung, D. Dickson, B. C. Giordano, M. E. Power, J. P. Ferrance, S. H. Feldman, P. M. Norris, and J. P. Landers. Microchip-based purification of dna from biological samples. *Anal Chem*, 75(8) :1880–6, 2003.

[49] R. P. Oda, M. A. Strausbauch, A. F. Huhmer, N. Borson, S. R. Jurrens, J. Craighead, P. J. Wettstein, B. Eckloff, B. Kline, and J. P. Landers. Infrared-mediated thermocycling for ultrafast polymerase chain reaction amplification of dna. *Anal Chem*, 70(20) :4361–8, 1998.

[50] A. T. Woolley, D. Hadley, P. Landre, A. J. deMello, R. A. Mathies, and M. A. Northrup. Functional integration of pcr amplification and capillary electrophoresis in a microfabricated dna analysis device. *Anal Chem*, 68(23) :4081–6, 1996.

[51] R. C. Anderson, X. Su, G. J. Bogdan, and J. Fenton. A miniature integrated device for automated multistep genetic assays. *Nucleic Acids Res*, 28(12) :E60, 2000.

[52] R.H. Liu, T. Nguyen, K. Schwarzkopf, H.S. Fuji, A. Petrova, T. Siuda, K. Peyvan, M. Bizak, D. Danley, and A. McShea. Fully integrated miniature device for automated gene expression dna microarray processing. *Anal. Chem.*, 78(6) :1980–1986, 2006.

[53] Z. Guttenberg, A. Rathgeber, S. Keller, J. O. Radler, A. Wixforth, M. Kostur, M. Schindler, and P. Talkner. Flow profiling of a surface-acoustic-wave nanopump. *Phys Rev E Stat Nonlin Soft Matter Phys*, 70(5 Pt 2) :056311, 2004.

[54] R. H. Liu, R. Lenigk, R. L. Druyor-Sanchez, J. Yang, and P. Grodzinski. Hybridization enhancement using cavitation microstreaming. *Anal Chem*, 75(8) :1911–7, 2003.

[55] Mark K. McQuain, Kevin Seale, Joel Peek, Timothy S. Fisher, Shawn Levy, Mark A. Stremler, and Frederick R. Haselton. Chaotic mixer improves microarray hybridization. *Analytical Biochemistry*, 325(2) :215–226, 2004.

[56] J. Liu, B. A. Williams, R. M. Gwirtz, B. J. Wold, and S. Quake. Enhanced signals and fast nucleic acid hybridization by microfluidic chaotic mixing. *Angew Chem Int Ed Engl*, 2006.

[57] N. B. Adey, M. Lei, M. T. Howard, J. D. Jensen, D. A. Mayo, D. L. Butel, S. C. Coffin, T. C. Moyer, D. E. Slade, M. K. Spute, A. M. Hancock, G. T. Eisenhoffer, B. K. Dalley, and M. R. McNeely. Gains in sensitivity with a device that mixes microarray hybridization solution in a 25-microm-thick chamber. *Anal Chem*, 74(24) :6413–7, 2002.

[58] C. W. Wei, J. Y. Cheng, C. T. Huang, M. H. Yen, and T. H. Young. Using a microfluidic device for 1 microl dna microarray hybridization in 500 s. *Nucleic Acids Res*, 33(8) :e78, 2005.

[59] B. P. Nelson, T. E. Grimsrud, M. R. Liles, R. M. Goodman, and R. M. Corn. Surface plasmon resonance imaging measurements of dna and rna hybridization adsorption onto dna microarrays. *Anal Chem*, 73(1) :1–7, 2001.

[60] V. Kanda, J. K. Kariuki, D. J. Harrison, and M. T. McDermott. Label-free reading of microarray-based immunoassays with surface plasmon resonance imaging. *Analytical Chemistry*, 76(24) :7257–7262, 2004.

[61] A. W. Peterson, L. K. Wolf, and R. M. Georgiadis. Hybridization of mismatched or partially matched dna at surfaces. *J Am Chem Soc*, 124(49) :14601–7, 2002.

[62] Y. Okahata, M. Kawase, K. Niikura, F. Ohtake, H. Furusawa, and Y. Ebara. Kinetic measurements of dna hybridization on an oligonucleotide-immobilized 27-mhz quartz crystal microbalance. *Anal Chem*, 70(7) :1288–96, 1998.

[63] M.F. Ali, R. Kirby, A.P. Goodey, M.D. Rodriguez, A.D. Ellington, D.P. Neikirk, and J.T. McDevitt. Dna hybridization and discrimination of single-nucleotide mismatches using chip-based microbead arrays. *Anal. Chem.*, 75(18) :4732–4739, 2003.

[64] A. Dodge, G. Turcatti, I. Lawrence, N. F. de Rooij, and E. Verpoorte. A microfluidic platform using molecular beacon-based temperature calibration for thermal dehybridization of surface-bound dna. *Analytical Chemistry*, 76(6) :1778–1787, 2004.

[65] A. W. Peterson, R. J. Heaton, and R. M. Georgiadis. The effect of surface probe density on dna hybridization. *Nucleic Acids Res*, 29(24) :5163–8, 2001.

[66] Sergei V. Tillib, Boris N. Strizhkov, and Andrei D. Mirzabekov. Integration of multiple pcr amplifications and dna mutation analyses by using oligonucleotide microchip. *Analytical Biochemistry*, 292(1) :155–160, 2001.

[67] Jean Taine and Jean-Pierre Petit. *Transferts Thermiques*. Sciences Sup. Paris, dunod edition, 2003.

[68] D. Erickson, D. Sinton, and D. Li. Joule heating and heat transfer in poly(dimethylsiloxane) microfluidic systems. *Lab Chip*, 3(3) :141–9, 2003.

[69] T. Yamamoto, T. Fujii, and T. Nojima. Pdms-glass hybrid microreactor array with embedded temperature control device. application to cell-free protein synthesis. *Lab Chip*, 2(4) :197–202, 2002.

[70] Jr. SantaLucia, J. A unified view of polymer, dumbbell, and oligonucleotide dna nearest-neighbor thermodynamics. *Proc Natl Acad Sci U S A*, 95(4) :1460–5, 1998.

[71] N. Peyret. *Prediction of Nucleic Acid Hybridization : Parameters and Algorithms*. Phd dissertation, Wayne State University, 2000.

[72] M. Zuker. Mfold web server for nucleic acid folding and hybridization prediction. *Nucleic Acids Res*, 31(13) :3406–15, 2003.

[73] G. Ocvirk, M. Munroe, T. Tang, R. Oleschuk, K. Westra, and D. J. Harrison. Electrokinetic control of fluid flow in native poly(dimethylsiloxane) capillary electrophoresis devices. *Electrophoresis*, 21(1) :107–15, 2000.

[74] A. Chatterjee, S. P. Moulik, P. R. Majhi, and S. K. Sanyal. Studies on surfactant-biopolymer interaction. i. microcalorimetric investigation on the interaction of cetyltrimethylammonium bromide (ctab) and sodium dodecylsulfate (sds) with gelatin (gn), lysozyme (lz) and deoxyribonucleic acid (dna). *Biophys Chem*, 98(3) :313–27, 2002.

[75] L. M. Wick, J. M. Rouillard, T. S. Whittam, E. Gulari, J. M. Tiedje, and S. A. Hashsham. On-chip non-equilibrium dissociation curves and dissociation rate constants as methods to assess specificity of oligonucleotide probes. *Nucleic Acids Res*, 34(3) :e26, 2006.

[76] R. D. Blake and S. G. Delcourt. Thermodynamic effects of formamide on dna stability. *Nucleic Acids Res*, 24(11) :2095–103, 1996.

[77] C. C. Chou, C. H. Chen, T. T. Lee, and K. Peck. Optimization of probe length and the number of probes per gene for optimal microarray analysis of gene expression. *Nucleic Acids Res*, 32(12) :e99, 2004.

[78] James A. Benn, Jenny Hu, Bradley J. Hogan, Rebecca C. Fry, Leona D. Samson, and Todd Thorsen. Comparative modeling and analysis of microfluidic and conventional dna microarrays. *Analytical Biochemistry*, 348(2) :284–293, 2006.

[79] Jr. SantaLucia, J. and D. Hicks. The thermodynamics of dna structural motifs. *Annu Rev Biophys Biomol Struct*, 33 :415–40, 2004.

[80] R. Owczarzy, Y. You, B. G. Moreira, J. A. Manthey, L. Huang, M. A. Behlke, and J. A. Walder. Effects of sodium ions on dna duplex oligomers : improved predictions of melting temperatures. *Biochemistry*, 43(12) :3537–54, 2004.

[81] J. G. Wetmur and N. Davidson. Kinetics of renaturation of dna. *Journal of Molecular Biology*, 31(3) :349, 1968.

[82] A. P. Williams, C. E. Longfellow, S. M. Freier, R. Kierzek, and D. H. Turner. Laser temperature-jump, spectroscopic, and thermodynamic study of salt effects on duplex formation by dgcatgc. *Biochemistry*, 28(10) :4283–91, 1989.

[83] J. R. Hutton. Renaturation kinetics and thermal stability of dna in aqueous solutions of formamide and urea. *Nucleic Acids Res*, 4(10) :3537–55, 1977.

[84] N. Zammatteo, L. Jeanmart, S. Hamels, S. Courtois, P. Louette, L. Hevesi, and J. Remacle. Comparison between different strategies of covalent attachment of dna to glass surfaces to build dna microarrays. *Anal Biochem*, 280(1) :143–50, 2000.

[85] J. L. Mergny and L. Lacroix. Analysis of thermal melting curves. *Oligonucleotides*, 13(6) :515–37, 2003.

[86] W. T. Liu, J. H. Wu, E. S. Li, and E. S. Selamat. Emission characteristics of fluorescent labels with respect to temperature changes and subsequent effects on dna microchip studies. *Appl Environ Microbiol*, 71(10) :6453–7, 2005.

[87] B. Valeur. *Invitation à la fluorescence moléculaire*. De boeck edition, 2004.

[88] A. V. Fotin, A. L. Drobyshev, D. Y. Proudnikov, A. N. Perov, and A. D. Mirzabekov. Parallel thermodynamic analysis of duplexes on oligodeoxyribonucleotide microchips. *Nucleic Acids Res*, 26(6) :1515–21, 1998.

[89] A. O. Crockett and C. T. Wittwer. Fluorescein-labeled oligonucleotides for real-time pcr : using the inherent quenching of deoxyguanosine nucleotides. *Anal Biochem*, 290(1) :89–97, 2001.

[90] F. Yu, D. Yao, and W. Knoll. Oligonucleotide hybridization studied by a surface plasmon diffraction sensor (spds). *Nucleic Acids Res*, 32(9) :e75, 2004.

[91] A. Halperin, A. Buhot, and E. B. Zhulina. Sensitivity, specificity, and the hybridization isotherms of dna chips. *Biophys J*, 86(2) :718–30, 2004.

[92] I. Langmuir. The adsorption of gases on plane surfaces of glass, mica, and platinum. *J. Am. Chem. Soc*, 40 :1399–1400, 1918.

[93] A. Vainrub and B. M. Pettitt. Coulomb blockage of hybridization in two-dimensional dna arrays. *Phys Rev E Stat Nonlin Soft Matter Phys*, 66(4 Pt 1) :041905, 2002.

[94] A. N. Frumkin. Influence of cation adsorption on the kinetics of electrode processes. *Transactions of the Faraday Society*, 55(1) :156–167, 1959.

[95] H. Diamant and D. Andelman. Kinetics of surfactant adsorption at fluid-fluid interfaces. *Journal of Physical Chemistry*, 100(32) :13732–13742, 1996.

[96] E. B. Khomyakova, E. V. Dreval, M. Tran-Dang, M. C. Potier, and F. P. Soussaline. Innovative instrumentation for microarray scanning and analysis : application for characterization of oligonucleotide duplexes behavior. *Cell Mol Biol (Noisy-le-grand)*, 50(3) :217–24, 2004.

[97] J.H. Watterson, P.A.E. Piunno, C.C. Wust, and U.J. Krull. Effects of oligonucleotide immobilization density on selectivity of quantitative transduction of hybridization of immobilized dna. *Langmuir*, 16(11) :4984–4992, 2000.

[98] A. Halperin, A. Buhot, and E. B. Zhulina. Brush effects on dna chips : thermodynamics, kinetics, and design guidelines. *Biophys J*, 89(2) :796–811, 2005.

[99] P. Gong, G.M. Harbers, and D.W. Grainger. Multi-technique comparison of immobilized and hybridized oligonucleotide surface density on commercial amine-reactive microarray slides. *Anal. Chem.*, 78(7) :2342–2351, 2006.

[100] Z. Guo, R. A. Guilfoyle, A. J. Thiel, R. Wang, and L. M. Smith. Direct fluorescence analysis of genetic polymorphisms by hybridization with oligonucleotide arrays on glass supports. *Nucleic Acids Res*, 22(24) :5456–65, 1994.

[101] M. S. Shchepinov, S. C. Case-Green, and E. M. Southern. Steric factors influencing hybridisation of nucleic acids to oligonucleotide arrays. *Nucleic Acids Res*, 25(6) :1155–61, 1997.

[102] R. Schlapak, P. Pammer, D. Armitage, R. Zhu, P. Hinterdorfer, M. Vaupel, T. Fruhwirth, and S. Howorka. Glass surfaces grafted with high-density poly(ethylene glycol) as substrates for dna oligonucleotide microarrays. *Langmuir*, 22(1) :277–85, 2006.

[103] R. J. Heaton, A. W. Peterson, and R. M. Georgiadis. Electrostatic surface plasmon resonance : direct electric field-induced hybridization and denaturation in monolayer nucleic acid films and label-free discrimination of base mismatches. *Proc Natl Acad Sci U S A*, 98(7) :3701–4, 2001.

[104] C. Gadgil, A. Yeckel, J. J. Derby, and W. S. Hu. A diffusion-reaction model for dna microarray assays. *Journal of Biotechnology*, 114(1-2) :31–45, 2004.

[105] U. Jonsson, L. Fagerstam, B. Ivarsson, B. Johnsson, R. Karlsson, K. Lundh, S. Lofas, B. Persson, H. Roos, I. Ronnberg, and et al. Real-time biospecific interaction analysis using surface plasmon resonance and a sensor chip technology. *Biotechniques*, 11(5) :620–7, 1991.

[106] D. G. Myszka, P. R. Arulanantham, T. Sana, Z. Wu, T. A. Morton, and T. L. Ciardelli. Kinetic analysis of ligand binding to interleukin-2 receptor complexes created on an optical biosensor surface. *Protein Sci*, 5(12) :2468–78, 1996.

[107] David G Myszka. Kinetic analysis of macromolecular interactions using surface plasmon resonance biosensors. *Current Opinion in Biotechnology*, 8(1) :50–57, 1997.

[108] Tamra Mason, Angel R. Pineda, Carla Wofsy, and Byron Goldstein. Effective rate models for the analysis of transport-dependent biosensor data. *Mathematical Biosciences*, 159(2) :123–144, 1999.

[109] D. G. Myszka, X. He, M. Dembo, T. A. Morton, and B. Goldstein. Extending the range of rate constants available from biacore : interpreting mass transport-influenced binding data. *Biophys J*, 75(2) :583–94, 1998.

[110] D. A. Edwards and S. A. Jackson. Testing the validity of the effective rate constant approximation for surface reaction with transport. *Applied Mathematics Letters*, 15(5) :547–552, 2002.

[111] D. A. Edwards. Refining the measurement of rate constants in the biacore. *J Math Biol*, 49(3) :272–92, 2004.

[112] D. A. Edwards. Estimating rate constants in a convection-diffusion system with a boundary reaction. *Journal of Applied Mathematics*, 63(1) :89–112, 1999.

[113] Thomas Gervais and Klavs F. Jensen. Mass transport and surface reactions in microfluidic systems. *Chemical Engineering Science*, 61(4) :1102–1121, 2006.

[114] P. Schaaf and J. Talbot. Surface exclusion effects in adsorption processes. *Journal of Chemical Physics*, 91(7) :4401–4409, 1989.

[115] R. Georgiadis, K.P. Peterlinz, and A.W. Peterson. Quantitative measurements and modeling of kinetics in nucleic acid monolayer films using spr spectroscopy. *J. Am. Chem. Soc.*, 122(13) :3166–3173, 2000.

[116] K.A. Peterlinz and R. Georgiadis. In situ kinetics of self-assembly by surface plasmon resonance spectroscopy. *Langmuir*, 12(20) :4731–4740, 1996.

[117] P. Schaaf and J. Talbot. Kinetics of random sequential adsorption. *Physical Review Letters*, 62(2) :175–178, 1989.

[118] L. K. Koopal and M. J. Avena. A simple model for adsorption kinetics at charged solid-liquid interfaces. *Colloids and Surfaces a-Physicochemical and Engineering Aspects*, 192(1-3) :93–107, 2001.

[119] A. E. Nkodo, J. M. Garnier, B. Tinland, H. Ren, C. Desruisseaux, L. C. McCormick, G. Drouin, and G. W. Slater. Diffusion coefficient of dna molecules during free solution electrophoresis. *Electrophoresis*, 22(12) :2424–32, 2001.

[120] Bernard Tinland, Alain Pluen, Jean Sturm, and Gilbert Weill. Persistence length of single-stranded dna. *Macromolecules*, 30 :5763–5765, 1997.

[121] T. A. Morton, D. G. Myszka, and I. M. Chaiken. Interpreting complex binding kinetics from optical biosensors : a comparison of analysis by linearization, the integrated rate equation, and numerical integration. *Anal Biochem*, 227(1) :176–85, 1995.

[122] L. Joss, T. A. Morton, M. L. Doyle, and D. G. Myszka. Interpreting kinetic rate constants from optical biosensor data recorded on a decaying surface. *Anal Biochem*, 261(2) :203–10, 1998.

[123] A. M. Laurent, M. Li, S. Sherman, G. Roizes, and J. Buard. Recombination across the centromere of disjoined and non-disjoined chromosome 21. *Hum Mol Genet*, 12(17) :2229–39, 2003.

[124] R Sachidanandam, D Weissman, SC Schmidt, JM Kakol, LD Stein, G Marth, S Sherry, JC Mullikin, BJ Mortimore, DL Willey, SE Hunt, CG Cole, PC Coggill, CM Rice, Z Ning, J Rogers, DR Bentley, PY Kwok, ER Mardis, RT Yeh, B Schultz, L Cook, R Davenport, M Dante, L Fulton, L Hillier, RH Waterston, JD McPherson, B Gilman, S Schaffner, WJ Van Etten, D Reich, J Higgins, MJ Daly, B Blumenstiel, J Baldwin, N Stange-Thomann, MC Zody, L Linton, ES Lander, D Altshuler, and International SNP Map Working Group. A map of human genome sequence variation containing 1.42 million single nucleotide polymorphisms. *Nature*, 409(6822) :928–933, 2001.

[125] K. Lindroos, S. Sigurdsson, K. Johansson, L. Ronnblom, and A. C. Syvanen. Multiplex snp genotyping in pooled dna samples by a four-colour microarray system. *Nucleic Acids Res*, 30(14) :e70, 2002.

[126] Ann-Christine Syvänen. From gels to chips : Minisequencing primer extension for analysis of point mutations and single nucleotide polymorphisms. *Human Mutation*, 13(1) :1–10, 1999.

[127] Thomas D Yager, Laurent Baron, Ruby Batra, Anne Bouevitch, David Chan, Karen Chan, Steve Darasch, Rod Gilchrist, Alex Izmailov, Jean-Michel Lacroix, Kelly Marchelleta, John Renfrew, Diane Rushlow, Eric Steinbach, Christopher Ton, Paul Waterhouse, Henryk Zaleski, James M Dunn, and John Stevens. High performance dna sequencing, and the detection of mutations and polymorphisms, on the clipper sequencer. *Electrophoresis*, 20(6) :1280–1300, 1999.

[128] W. M. Howell, M. Jobs, U. Gyllensten, and A. J. Brookes. Dynamic allele-specific hybridization. a new method for scoring single nucleotide polymorphisms. *Nat Biotechnol*, 17(1) :87–8, 1999.

[129] H. Dai, M. Meyer, S. Stepaniants, M. Ziman, and R. Stoughton. Use of hybridization kinetics for differentiating specific from non-specific binding to oligonucleotide microarrays. *Nucleic Acids Res*, 30(16) :e86, 2002.

[130] K. Tawa and W. Knoll. Mismatching base-pair dependence of the kinetics of dna-dna hybridization studied by surface plasmon fluorescence spectroscopy. *Nucleic Acids Res*, 32(8) :2372–7, 2004.

[131] H. Urakawa, P. A. Noble, S. El Fantroussi, J. J. Kelly, and D. A. Stahl. Single-base-pair discrimination of terminal mismatches by using oligonucleotide microarrays and neural network analyses. *Appl Environ Microbiol*, 68(1) :235–44, 2002.

[132] T. Xie, S. L. Ho, and O. C. Ma. High resolution single strand conformation polymorphism analysis using formamide and ethidium bromide staining. *Mol Pathol*, 50(5) :276–8, 1997.

[133] J. Bishop, S. Blair, and A. M. Chagovetz. A competitive kinetic model of nucleic acid surface hybridization in the presence of point mutants. *Biophys J*, 90(3) :831–40, 2006.

[134] Ying Zhang, Daniel A. Hammer, and David J. Graves. Competitive hybridization kinetics reveals unexpected behavior patterns. *Biophys. J.*, 89(5) :2950–2959, 2005.

[135] Bjorn Persson, Karin Stenhag, Peter Nilsson, Anita Larsson, Mathias Uhlen, and Per-Ake Nygren. Analysis of oligonucleotide probe affinities using surface plasmon resonance : A means for mutational scanning. *Analytical Biochemistry*, 246(1) :34–44, 1997.

[136] Emmanuelle Haquet. *Recombinaison entre chromosomes non-disjoints dans la trisomie 21 et corrélations génotypes/phénotypes dans le syndrôme de Down.* PhD thesis, Université de Montpellier II, 2006.

[137] S. Rollinson, J. M. Allan, G. R. Law, P. L. Roddam, M. T. Smith, C. Skibola, A. G. Smith, M. S. Forrest, K. Sibley, R. Higuchi, S. Germer, and G. J. Morgan. High-throughput association testing on dna pools to identify genetic variants that confer susceptibility to acute myeloid leukemia. *Cancer Epidemiol Biomarkers Prev*, 13(5) :795–800, 2004.

[138] J. Tost, J. Dunker, and I. G. Gut. Analysis and quantification of multiple methylation variable positions in cpg islands by pyrosequencing. *Biotechniques*, 35(1) :152–6, 2003.

Index

Intégration de puce à ADN dans un microsystème fluidique

Ce travail de thèse présente la conception et la réalisation de dispositifs microfluidiques en PDMS (Polydiméthylsiloxane) pour l'intégration d'analyses biologiques. Dans un premier temps, des outils microfluidiques sont construits et améliorés dans ce but : une méthode de pompage passif et de mise en oeuvre du PDMS a fait l'objet d'un dépôt de brevet. Les micro-pompes, éléments clés d'une intégration poussée, sont étudiées expérimentalement et théoriquement, menant à un modèle prédictif basé sur une équivalence électrique. Ce travail a été publié dans *Journal of Applied Physics*. La dispersion hydrodynamique, diluant les échantillons lors de leur transport est caractérisée. De cette analyse, une nouvelle méthode de génération de gradients de concentration est conçue et testée expérimentalement. Fort de ces développements, une plate-forme microfluidique originale intégrant des puces à ADN est fabriquée en une version de laboratoire et une version portable. Grâce à ce dispositif, les connaissances de la réaction d'hybridation sur une surface, base des puces à ADN, sont complétées par des mesures comparées de courbes de fusion et un modèle de couplage réaction-diffusion-advection est étendu expérimentalement au cas des puces à ADN. Finalement dans le cadre d'une collaboration avec l'IGH (Institut de Génétique Humaine) de Montpellier, deux méthodes originales de dosage d'allèles pour la trisomie 21 sont testées et des expériences sur des échantillons biologiques sont en cours de préparation. En conclusion, cette thèse a donné lieu au dépôt d'un brevet et à la publication de deux articles. Elle aura abouti à la mise en oeuvre de méthodes et approches originales basées sur la technologie microfluidique, appliquées à différents domaines (dispersion, pompage, puce à ADN).

Mots clés :

puce à ADN, microfluidique, micropompe, dispersion de Taylor-Aris, hybridation, PDMS

DNA microarrays Integrated in a Microfluidic Device

This thesis deals with the design and the fabrication of microfluidic devices in PDMS (Polydimethylsiloxane) for biological applications. A microfluidic environment is first fabricated and basic tools are improved : a passive method that enables drawing up liquids in PDMS micro-channels is presented and was patented. Micro-pumps, a key element for complex architecture are studied from both an experimental and a theoretical point of view. Thanks to this study, performances are improved and a predictive model based on an electronic equivalence is described (published in *Journal of Applied Physics*). Besides, hydrodynamic dispersion that leads to unwilling dilution of analyte during transport is studied for the particular case of micro-channels. From this study, a new method of production of concentration gradients is both theoretically and experimentally described. From this work, an original microfluidic plate-form that integrates DNA microarrays in a precisely controlled environment in term of temperature, micro-flow and real time measurements is described. Thanks to this new set up, DNA hybridization on chip and under bulk conditions are compared and results complete recent developments on the physic of hybridization on chip. Moreover, a model that describes the coupling phenomena of reaction-diffusion-advection is experimentally extended to DNA microarrays. Finally in collaboration with IGH (Institut de Génétique Humaine) in Montpellier, two new methods that measure allele ratio for the genetic disease "Down syndrome" are tested experimentally and experiments on biological samples are under process. As a conclusion, new microfluidics devices are presented here leading to original approaches for biological applications.

Key words :

DNA microarray, microfluidics, micropump, Taylor-Aris dispersion, hybridization, PDMS